iScience

Article

Divergent brain solute clearance in rat models of cerebral amyloid angiopathy and Alzheimer's disease

Graphical abstract

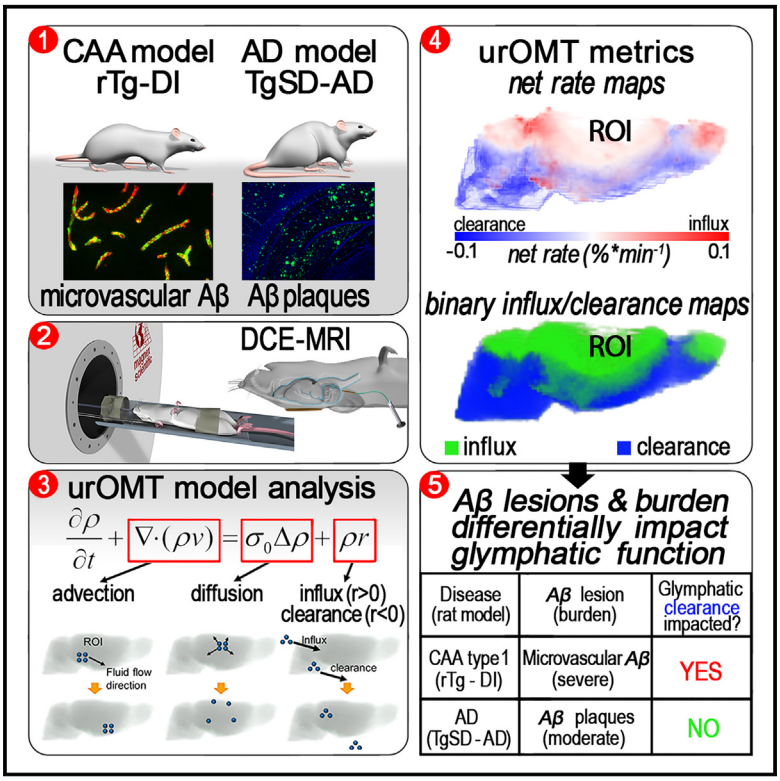

Highlights

- UrOMT analysis allows for quantification of glymphatic influx/clearance net rates
- Microvascular amyloid beta (Aβ) deposition decreases glymphatic solute clearance
- Moderate Aβ plaque load in an AD rat model does not affect clearance
- Aβ lesions and burden differentially impact glymphatic clearance function

Authors

Sunil Koundal, Xinan Chen, Zachary Gursky, ..., Rena Elkin, Allen Tannenbaum, Helene Benveniste

Correspondence

helene.benveniste@yale.edu

In brief

Biological sciences; Neuroscience

Koundal et al., 2024, iScience 27, 111463
December 20, 2024 © 2024 The Author(s). Published by Elsevier Inc.
https://doi.org/10.1016/j.isci.2024.111463

CellPress

iScience

CellPress
OPEN ACCESS

Article

Divergent brain solute clearance in rat models of cerebral amyloid angiopathy and Alzheimer's disease

Sunil Koundal,[1,8] Xinan Chen,[2,8] Zachary Gursky,[1] Hedok Lee,[1] Kaiming Xu,[1,3] Feng Liang,[4] Zhongcong Xie,[4] Feng Xu,[5] Hung-Mo Lin,[1] William E. Van Nostrand,[5] Xianfeng Gu,[3,6] Rena Elkin,[2] Allen Tannenbaum,[3,6] and Helene Benveniste[1,7,9,*]

[1]Department of Anesthesiology, Yale School of Medicine, New Haven, CT 06510, USA
[2]Department of Medical Physics, Memorial Sloan Kettering Cancer Center, New York City, NY 10065, USA
[3]Department of Applied Mathematics & Statistics, Stony Brook University, Stony Brook, NY 11794, USA
[4]Department of Anesthesia, Critical Care and Pain Medicine, Massachusetts General Hospital, Harvard Medical School, Charlestown, MA 02114, USA
[5]George and Anne Ryan Institute for Neuroscience and the Department of Biomedical and Pharmaceutical Sciences, University of Rhode Island, Kingston, RI 02906, USA
[6]Departments of Computer Science, Stony Brook University, Stony Brook, NY 11794, USA
[7]Department of Biomedical Engineering, Yale School of Medicine New Haven, New Haven, CT 06510, USA
[8]These authors contributed equally
[9]Lead contact
*Correspondence: helene.benveniste@yale.edu
https://doi.org/10.1016/j.isci.2024.111463

SUMMARY

Brain waste clearance from the interstitial fluid environment is challenging to measure, which has contributed to controversy regarding the significance of glymphatic transport impairment for neurodegenerative processes. Dynamic contrast enhanced MRI (DCE-MRI) with cerebrospinal fluid administration of Gd-tagged tracers is often used to assess glymphatic system function. We previously quantified glymphatic transport from DCE-MRI data utilizing regularized optimal mass transport (rOMT) analysis, however, information specific to glymphatic clearance was not directly derived. To fill this knowledge gap, we here implemented unbalanced rOMT analysis which allows for assessment of both influx and clearance. Dynamic influx/clearance brain maps were derived from rTg-DI rats with cerebral amyloid angiopathy (CAA) and TgSD-AD rats with Alzheimer's disease (AD). The rTg-DI rats with severe CAA disease exhibited abnormal influx/clearance kinetics, while TgSD-AD rats with a moderate Aβ plaque load exhibited normal transport suggesting that different Aβ lesions and their overall burden differentially impact glymphatic system function.

INTRODUCTION

A hallmark of Alzheimer's disease (AD) includes the presence of fibrillar amyloid beta (Aβ) aggregates in the form of parenchymal plaques[1,2] and in cerebral amyloid angiopathy (CAA) fibrillar Aβ deposits along the microvasculature (type 1) or within the vessel wall (type 2).[3] Impairment of Aβ waste clearance via the brain's glymphatic system has been linked to the pathogenesis of both AD[4–8] and CAA.[9–11] According to the glymphatic system model, cerebrospinal fluid (CSF) circulates in the subarachnoid space and enters the brain parenchyma via channels along the arteries from where it mixes with interstitial fluid (ISF) facilitating waste removal via peri-venous channels in a process referred to as ''clearance''.[12–14] The peri-venous outflow of brain fluids containing waste collects into the meningeal lymphatics that drain into the cervical lymph nodes and systemic circulation.[8,15–18] It has been hypothesized that suppression of glymphatic transport due to age-related changes in aquaporin 4 water (AQP4) channel expression on astrocytic endfeet and neuroinflammation contributes to Aβ clearance impairment, thereby promoting oligomerization and fibrillar Aβ formation in the form of AD and/or CAA.[4,19,20] In support of this concept, solute clearance, as measured by injecting Aβ or inulin locally into the cortex and quantifying the percentage remaining in the brain after a given time period, was shown to be reduced in aging mice[19] and in APP/PS1 AD mice.[4] Other studies have reported decreased uptake of tracers from CSF into brain parenchyma in rodent models of AD as well as CAA, implying impaired glymphatic transport.[8,11]

We previously introduced dynamic contrast-enhanced MRI (DCE-MRI) with administration of Gd-tagged tracers into CSF for tracking glymphatic transport.[21,22] Over the past years, we evolved data-driven computational fluid dynamic models based on regularized optimal mass transport (rOMT) theory to characterize solute transport from experimentally acquired DCE-MRI brain data.[11,23–25] Specifically, the rOMT model includes an advection-diffusion equation from fluid dynamics to describe the advective (bulk flow) and diffusive behaviors of solute

This is an open access article under the CC BY-NC-ND license (http://creativecommons.org/licenses/by-nc-nd/4.0/).

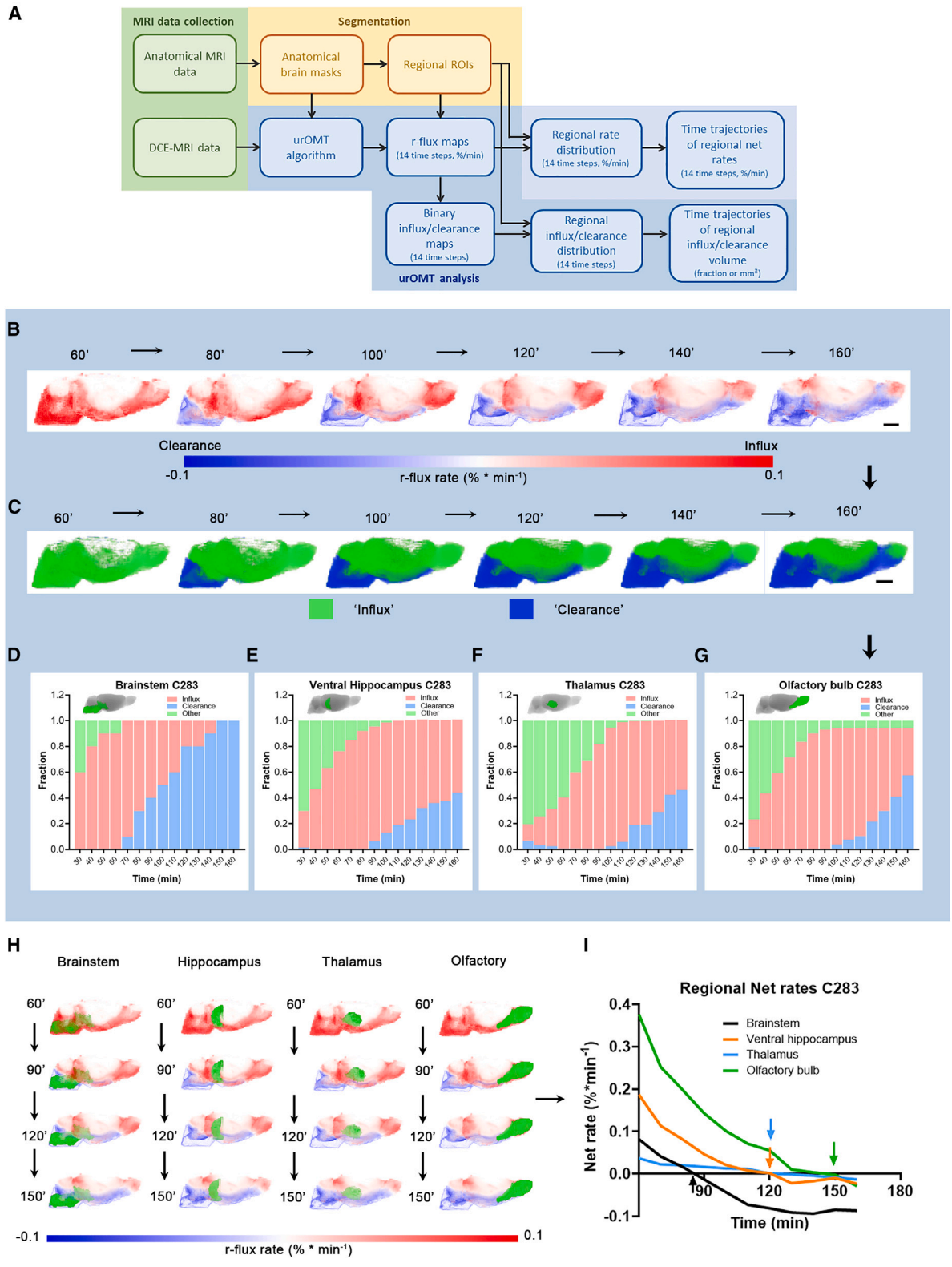

(legend on next page)

transport, under the assumption that the total mass of the contrast agent is conserved over time and that the total kinetic energy for the dynamic transportation of deforming images is minimized.[11,14] From the rOMT analysis, we computed several quantitative metrics describing solute transport in the local tissue environment including solute speed and Peclet number, albeit not clearance rates.[26] The total mass conservation constraint of the rOMT model restricts its application to analyzing data within a time window wherein the Gd-tracer level in brain parenchyma is relatively stable. In this work, we applied an extended version of the rOMT model, called the "unbalanced" regularized OMT (urOMT) model, where a source term is incorporated in the formulation enabling the assessment of influx/clearance in the local tissue environment from DCE-MRI images.[27] Consequently, the total mass conservation constraint is lifted to allow for emergence/removal of mass associated with temporal changes in the net amount of mass in a region, and the urOMT model is applicable to a broader time window as well as enabling the assessment of influx/clearance in the local tissue environment from DCE-MRI images. We applied the urOMT model to analyze DCE-MRI brain data acquired in 9-month-old transgenic (rTg-DI) CAA rats and 12-month-old TgSD-AD rats with the objective to evaluate glymphatic influx/clearance kinetics across two distinct pathologies: brain parenchymal Aβ plaques in the setting of AD versus microvascular Aβ in rTg-DI rats with CAA type 1.

We first demonstrate that the spatiotemporal patterns of glymphatic influx and clearance can be visualized and quantified from the so-called *r-flux* maps derived by the urOMT analysis. In the normal rat brain, solute clearance–based on the *r-flux* maps–commences ~60 min after CSF administration of the Gd-tracer and initially dominates in regions near the skull base. Further, in 9-month-old rTg-DI rats with severe stage CAA, urOMT analysis showed that trends in influx and clearance were significantly time-delayed in brain regions with high microvascular Aβ burden compared to control WT rats, congruent with previously reported data of time-delayed drainage to the cervical lymph nodes in the same rat model.[11] Notably, the same influx and clearance metrics by urOMT were observed to be within normal range in 12-month-old TgSD-AD rats with a moderate Aβ plaque burden, including in the ventral hippocampus. The urOMT results of abnormal influx/clearance kinetics in rTg-DI rats and normal transport in TgSD-AD rats were validated by corresponding Gd-tracer uptake results in the preselected regions of interest showing similar trends of glymphatic transport changes across the groups. Based on these new results, we propose that different pathological Aβ lesions as well as their overall tissue burden differentially impact glymphatic system function. We also propose that the computational urOMT model for analyzing real-time local solute transport in the brain might be useful for studying glymphatic system function including solute clearance based on DCE-MRI data.

RESULTS

Overview of influx and clearance metrics derived by urOMT analysis

The urOMT model utilized in this study is a data-driven approach for inferring apparent flow behavior that allows for characterizing solute influx and clearance kinetics in the whole brain as well as regionally, based on DCE-MRI data.[27] We were able to quantify influx and clearance kinetics with the urOMT model because a source term that describes the influx and clearance dynamics was added to the previous rOMT model where a positive source indicates influx and a negative source indicates clearance. As a point of clarity, we highlight the following subtle distinction between the physical mechanisms of influx/clearance and the apparent influx/clearance as captured in the DCE-MRI data. Physically, influx of tracer into the brain occurs via the CSF Gd tracer injection. Tracer then moves about the system until clearance occurs via the removal/clearance of Gd exiting the brain or region of interest (ROI). Due to imaging limitations and the apparent nature of the transport (see Discussion and Limitations of the study for more details), the Gd tracer, as captured in the DCE-MRIs, may appear to instantaneously emerge/disappear in a particular voxel or region of the brain. In such cases, it may not be possible to infer exactly where the tracer came from or went, but it is still possible to infer regional influx/clearance. Thus, from the data-driven modeling perspective, influx/clearance described by the source term indicates locally detected uptake/loss of tracer resulting from the physical influx/clearance that is not explained by the advective and diffusive transport. As such, the urOMT model incorporates three types of tracer transport motions including advection, diffusion, and influx/clearance.[27] Influx/clearance represents the transport (at the minute level) of the solute into/out of a voxel or brain region. The three different tracer movements independently contribute to the total transport in the local tissue environment (For more details see STAR Methods and the Discussion sections).

We first provide a brief overview of the quantitative metrics derived from the urOMT analysis of DCE-MRI data used in our study and illustrate the processing pipeline via an example from a single healthy rat in Figure 1. Specifically, 14 temporal 3D whole-brain maps of a metric referred to as "*r-flux*" are

Figure 1. Metrics derived with urOMT analysis

(A) Overview of data analysis and metrics derived from the urOMT analysis via *r-flux* maps.

(B) A representative time series of *r-flux* brain maps from a single normal rat (only 6 out of 14 time-steps are shown). Positive *r-flux* values in red color denote glymphatic influx and negative *r-flux* values in blue indicate clearance (see STAR Methods for details). Scale bar = 3 mm.

(C) Corresponding binary brain maps with the tissue *volume* exhibiting influx in green and clearance in blue. Scale bar = 3 mm.

(D–G) Graphs showing the time-trajectories of influx and clearance in different brain regions. The regional volume fractions of influx and clearance are shown in pink and blue, respectively, and the remaining fraction in green in four pre-selected brain regions. All brain image data are presented in the sagittal view plane.

(H) Limited time series of *r-flux* maps highlighting the regions of interest.

(I) Corresponding time-courses of net rate changes in the four brain regions from a single rat example. For each brain region, the arrows indicate the time where net influx = net clearance.

derived from the urOMT analysis, with each map time-averaged over 10-min intervals which altogether covers the experimental time window from 30 min →160 min after the start of gadoteric acid (Gd-DOTA) infusion into CSF.[27] The *r-flux* maps exhibits the spatiotemporal patterns of influx and clearance with positive *r-flux* values representing influx rates, while negative *r-flux* values represent clearance. As shown in Figure 1A, when combining the corresponding anatomical MRI data acquired for each rat with post-processing of the urOMT analysis, *r-flux* maps can extract information on (1) regional changes in solute influx and clearance rates which are converted into local 'net' rates in units of %*min^{-1} and (2) regional changes in solute influx and clearance volumes which are converted into fractional units or mm^3. Figure 1B shows an example of a time series of *r-flux* maps from the brain of a normal rat, in which the voxels are color coded so that influx rates are displayed in red color tones and clearance rates in blue color tones. As shown, in the first hour, positive *r-flux* values– signifying influx of the Gd-DOTA–dominate and progress in a typical centripetal glymphatic transport pattern previously described for both rodent and human brain based on DCE-MRI after CSF Gd-DOTA administration.[21,22,28,29] Note that over time, the red colors fade in the tissue signifying declining rates of influx and convert to blue color tones when clearance in the tissue take over (Figure 1B). Accordingly, the *r-flux* maps indicate that influx rates are initially high and later decline when clearance commences at ~70–80 min implying an overall gradual transitional Gd-DOTA transport process of intense influx → mild influx → mild clearance → intense clearance (Figure 1B).

We converted the *r-flux* maps into binary maps of tissue exhibiting influx or clearance by differently color coding influx voxels (*r-flux* values >0.0001%*min^{1}) and clearance voxels (*r-flux* values < −0.0001%*min^{1}) for more straightforward visualization of the spatial distribution patterns of influx and clearance in the brain. As expected, the binary maps depict influx/clearance information similarly to the *r-flux* rate maps by showing that influx in the brain parenchyma dominates over the first ~1h, and clearance emerges at ~70–80 min in tissue regions close to the skull base (Figure 1C). The binary maps were used to quantify volume fractions of influx/clearance in a given ROI by counting the number of influx/clearance voxels and dividing by the total number of voxels in the ROI, which if extracted at different timepoints can derive the corresponding time-trajectories. The graphs of the volume fractional time-trajectories from four different brain regions are shown in Figures 1D–1G. Specifically, for each time point the graphs show the tissue fraction of the ROI exhibiting influx and clearance in pink and blue colors, respectively, and the remaining tissue fraction wherein the *r-flux* values were below the threshold level is colored in green (Figures 1D–1G). From these graphs it is evident that in the brainstem, clearance (blue) emerges early and rises sharply (Figure 1D) while in the ventral hippocampus (Figure 1E), thalamus (Figure 1F), and olfactory bulb (Figure 1G) clearance is slower to emerge and rise. The binary ROI data derived from the *r-flux* maps is in agreement with previous reports of varying glymphatic transport across brain regions.[22]

In addition to volume, another metric derived from the *r-flux* maps pertains to the regional *net* rates. For a given ROI, the regional *net* rate is calculated as the spatial average of all *r-flux* rates within the ROI (Figure 1H), which if extracted at the different time points yield the corresponding time-trajectories. As has been reported previously, glymphatic transport by DCE-MRI and CSF administration of Gd-DOTA requires time to distribute into the brain parenchyma. Here, we therefore focused on time steps from ≥60 min after CSF administration of Gd-DOTA where most ROIs have taken up the Gd-tagged tracer. Figure 1I shows the time time-trajectories of the net rates derived from the brainstem, ventral hippocampus, thalamus, and olfactory bulb. Note that in all the regions the net rates decline over time, indicating a gradual switch of transport mode from influx to clearance with the net value decreasing from positive to negative. Further, for the four regions, the time where the net rate = 0 (i.e., influx = clearance) occurs at different times after CSF administration of Gd-DOTA (Figure 1I, arrows) implying that the corresponding transport kinetics vary across brain regions. Specifically, based on this data it is evident that clearance *exceeds* influx in the brainstem at 90 min and in the ventral hippocampus at ~130 min (Figure 1I). The data analysis approach presented in Figure 1 was applied to analyze influx and clearance kinetics in rat cohorts exhibiting either CAA or AD pathology and will be presented below.

Influx and clearance kinetics are abnormal and time-delayed in CAA type 1

For the CAA studies, we used the transgenic rat (rTg-DI) line, which expresses human Swedish/Dutch/Iowa vasculotropic mutant amyloid-beta precursor protein (AβPP) causing Aβ deposition along the capillaries.[30–32]. The age-dependent time trajectory of cerebral vascular pathology in this model has been well-documented.[30,31,33–36] In rTg-DI rats capillary CAA first emerges in the cortex, hippocampus, and thalamus starting at 3 months (M) of age. At 6 M, capillary CAA becomes more extensive in all brain regions and vascular lesions including cerebral microhemorrhages and vessel occlusions begin to emerge. At 9–12 M, the pathology in CAA rTg-DI rats becomes very severe and the animals become moribund. Accordingly, the trajectory of disease in this model is as follows: 3 months (emergent), 6 months (mid-level), and 9–12 months (severe, end-stage). To study influx and clearance kinetics, 9-month-old WT ($N = 7$) and CAA rTg-DI ($N = 8$) rats underwent DCE-MRI with CSF Gd-DOTA administration under anesthesia. Based on our previous data in 12-month-old rTg-DI rats,[11] we initially hypothesized that urOMT analysis of DCE-MRI data of 9 M rTg-DI rats would exhibit impaired influx/clearance kinetics. Briefly, for these experiments the rats were anesthetized with dexmedetomidine combined with low-dose isoflurane, and Gd-DOTA (1:37 dilution) was administered into the CSF via the cisterna magna during DCE-MRI imaging.[11,37] Each rat's DCE-MRI data was analyzed by the urOMT computational pipeline according to Figure 1. First, we show that the brain-wide changes via the binary maps from WT rats demonstrated normal progression of tissue influx with clearance emerging at ~70–80 min at the level of the brainstem and progressing toward the olfactory bulb (representative example of a WT rat is shown in Figure 2D). However, for the CAA rTg-DI rats, the brain-wide tissue influx was reduced over the first hour, and clearance was time-delayed when compared to WT

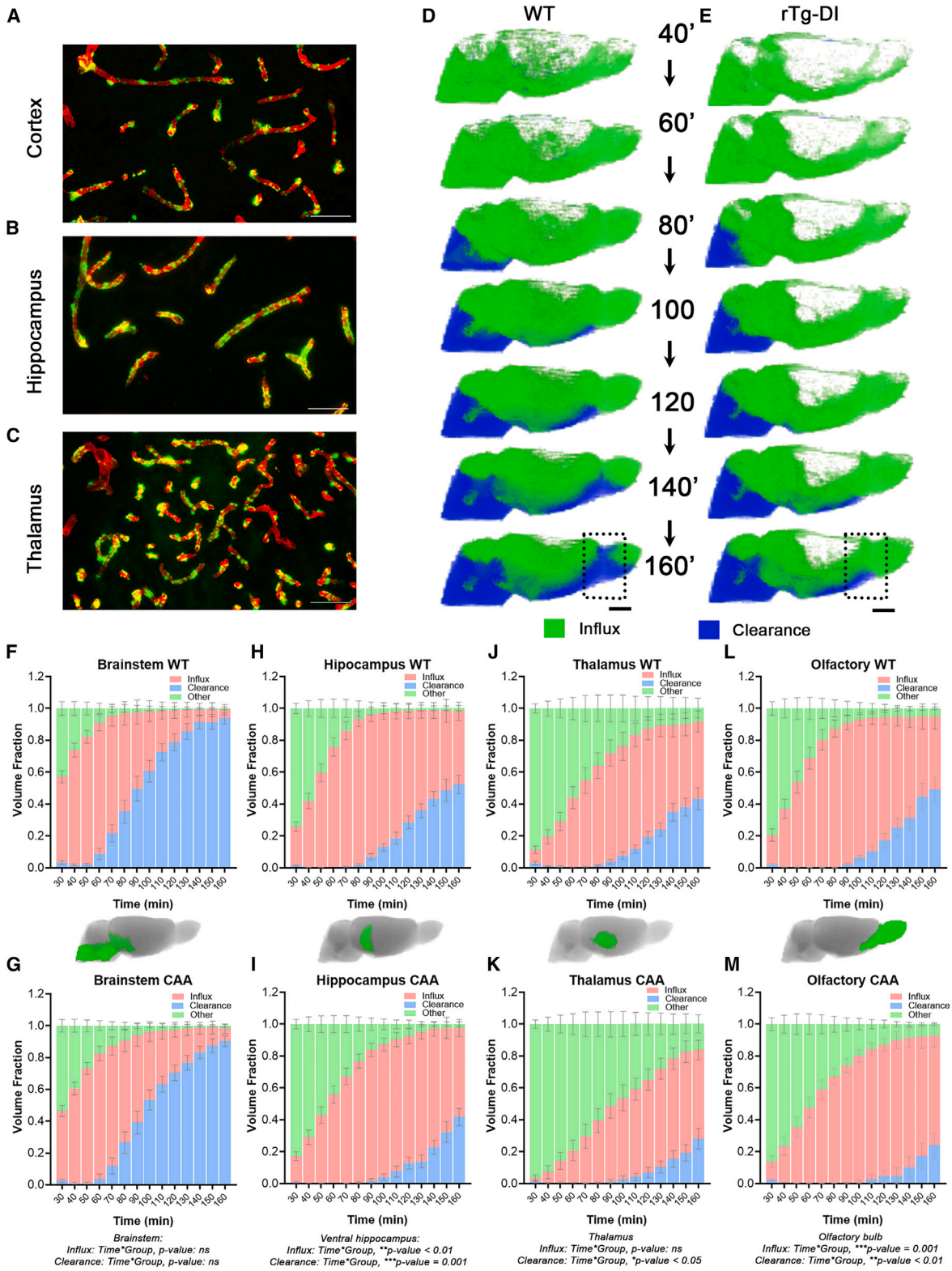

Figure 2. Microvascular fibrillar Aβ is linked to slower solute influx and clearance

(A–C) The microvascular amyloid deposits are present in cortex (A), hippocampus (B) and thalamus (C) of 9-month-old rTg-DI rats. Fibrillar amyloid beta was visualized by thioflavin-S and cerebral blood vessels by collagen IV. Scale bars = 50 μm.

(legend continued on next page)

(representative example of binary maps from a rTg-DI rats is shown in Figure 2E). Specifically, in the olfactory bulb, clearance was evident at ~140 min in the WT but not in the rTg-DI rat implying delayed or impaired transport kinetics (dashed black boxes in Figures 2D and 2E). The graphs depicting the regional binary influx/clearance time trajectories from the WT and rTg-DI cohorts focused on the brainstem, ventral hippocampus, thalamus, and olfactory bulb are shown in Figures 2F-M. The graphs display the regional volume fractions exhibiting influx and clearance in pink and blue colors, respectively, and the remaining tissue where *r-flux* values are below threshold in green. A linear mixed model for repeated measures (LMM-RM) with Bonferroni adjustment for multiple comparisons was utilized to assess differences within and across groups (WT vs. rTg-DI). There were no statistically significant differences neither in solute influx nor clearance transport in the brainstem across the two groups (Figures 2F and 2G, time*group p-value >0.05). However, significant influx differences were documented in the ventral hippocampus (time*group p-value = 0.002) (Figures 2H and 2I). Specifically, in the ventral hippocampus of WT rats, influx volume peaked at ~100 min and at ~140 min in rTg-DI rats (Figures 2F and 2G). In the hippocampus, the influx time-delay in rTg-DI rats was also reflected in the time-trends in clearance which was significantly different from the WT cohort (time*group p-value = 0.001). In the thalamus where Aβ deposits are severe in the 9-month-old rTg-DI rats tissue clearance was also significantly time-delayed (time*group p-value = 0.011) in comparison to the WT rats (Figures 2J and 2K). The olfactory bulb also exhibited abnormal transport kinetics, and the time trajectories of influx (time*group p-value = 0.001) and clearance (time*group p-value = 0.009) were significantly delayed in the rTg-DI rats (Figure 2L, 2M).

To further validate the results derived from the binary maps via urOMT analysis, we also assessed regional glymphatic transport in the brain tissue of the WT and rTg-DI rats using the more conventional Gd-DOTA uptake measure.[8,13,19,38,39] The analysis of the DCE-MRI data from the two groups (Figures S1A and S1B) confirmed that glymphatic transport as measured by the regional time-trajectories of Gd-DOTA uptake - "% signal from baseline" - was significantly altered in the ventral hippocampus (time*group, ***p-value <0.0001) of rTg-DI rats compared to WT (Figure S1D) but not in the brainstem (Figure S1C, time*group, p-value >0.05). The thalamus exhibited a trend of slower Gd-DOTA uptake in rTg-DI compared to WT rats. However, the regional signal was lower and overall, noisier when compared to the other brain regions and differences were not statistically significant (time*group, p-value = 0.128, Figure S1E). Finally, the time signal curves of Gd-DOTA transport in the olfactory bulb revealed time-delayed and decreased uptake in the rTg-DI compared to WT rats (time*group, p-value = 0.023, Figure S1F).

We next looked at the corresponding time-trends of the regional net rates derived from the *r-flux maps*. The net rates inform on the overall effect of transport in a given region, i.e., if the net rate is positive, net influx in region dominates over net clearance, and vice versa. In the brainstem there were no significant differences in the time varying trends of net rates across WT and rTg-DI rats (Figure 3A). However, the corresponding time-trends of net rates in the ventral hippocampus (Figure 3B) revealed that the time where net clearance exceeded net influx was time-delayed in rTg-DI rats which was also the case for the thalamus region (Figure 3C) and olfactory bulb (Figure 3D). Specifically, statistical analysis showed that for rTg-DI rats in the ventral hippocampus net clearance commenced with a delay of 20 min when compared to WT rats (WT (N = 7) clearance time = 121.4 ± 7.3 min vs. rTg-DI (N = 8) clearance time = 143.7 ± 7.0 min, mean difference = −22.3, 95% CI = [-44.4, −0.2] min, p-value = 0.048). Similarly, for the thalamus net clearance was also significantly time-delayed (WT (N = 7) clearance time = 125.7 ± 6.1 min vs. rTg-DI (N = 8) clearance time = 156.2 ± 5.1 min, mean difference = −30.5, 95% CI = [-45.6, −14.4] min, p-value = 0.002). For the olfactory bulb net clearance also commenced with a time delay in the CAA cohort (WT (N = 7) clearance time = 142.9 ± 6.1 min vs. rTg-DI (N = 8) clearance time = 158.8 ± 1.3 min, mean difference = −15.9, 95% CI = [-30.8, −1.0] min, p-value = 0.039). Collectively, from these data, we concluded that influx and clearance kinetics as defined by urOMT r-*flux* maps were significantly time-delayed in CAA type 1 implying impaired glymphatic function. We also concluded that the regional urOMT influx/clearance results were partly supported by the corresponding Gd-DOTA uptake measures although this metric does not directly inform on solute clearance.

TgSD-AD rats with a moderate Aβ plaque burden exhibit normal glymphatic influx and clearance kinetics

To characterize glymphatic influx and clearance kinetics in AD utilizing urOMT analysis, we chose the TgF344-AD rat model expressing familial AD mutant human amyloid precursor protein (*APPsw*) and presenilin 1 (*PS1ΔE9*) genes which develops Aβ plaques as well as endogenous hyperphosphorylated tau.[40] When compared to the rTg-DI rat model, the TgSD-AD rats are a model of more slowly progressive AD-like pathology presenting with abundant parenchymal Aβ plaques. Specifically, the trajectory of AD pathology in this model is more time-delayed compared to the rTg-DI model. Plaques first emerge in this model at ~6 M of age.[40] At 12–14 M, plaque pathology becomes more widespread and plaque-associated p-tau pathology becomes evident. At 18 + M of age, plaque pathology becomes very severe. Accordingly, the trajectory of disease in this model is 6 M (emergent), 12–16 M (mid-level), and 18 + M (severe, end-stage). To better evaluate influx/clearance metrics in AD with the

(D, E) Representative binary maps from a 9-month-old WT (D) and Tg-DI (E) rat showing the time varying trends in tissue exhibiting influx (green) or clearance (blue). Scale bars = 3mm.

(F–M) Graphs showing the time-trajectories of influx and clearance as fractional volumes from four different brain regions across WT (N = 7) and rTg-DI (N = 8) rats. The fractional volume data are group averages ±SEM. For each region, p-values for group*time interaction effects for influx and clearance extracted using a linear mixed model for repeated measures with independent variables including strain, time and the time × strain interaction were fit to compare the mean differences of different outcomes between strains and between time points are indicated below the graphs; ns = non-significant, *p < 0.05, **p < 0.01; ***p = 0.001.

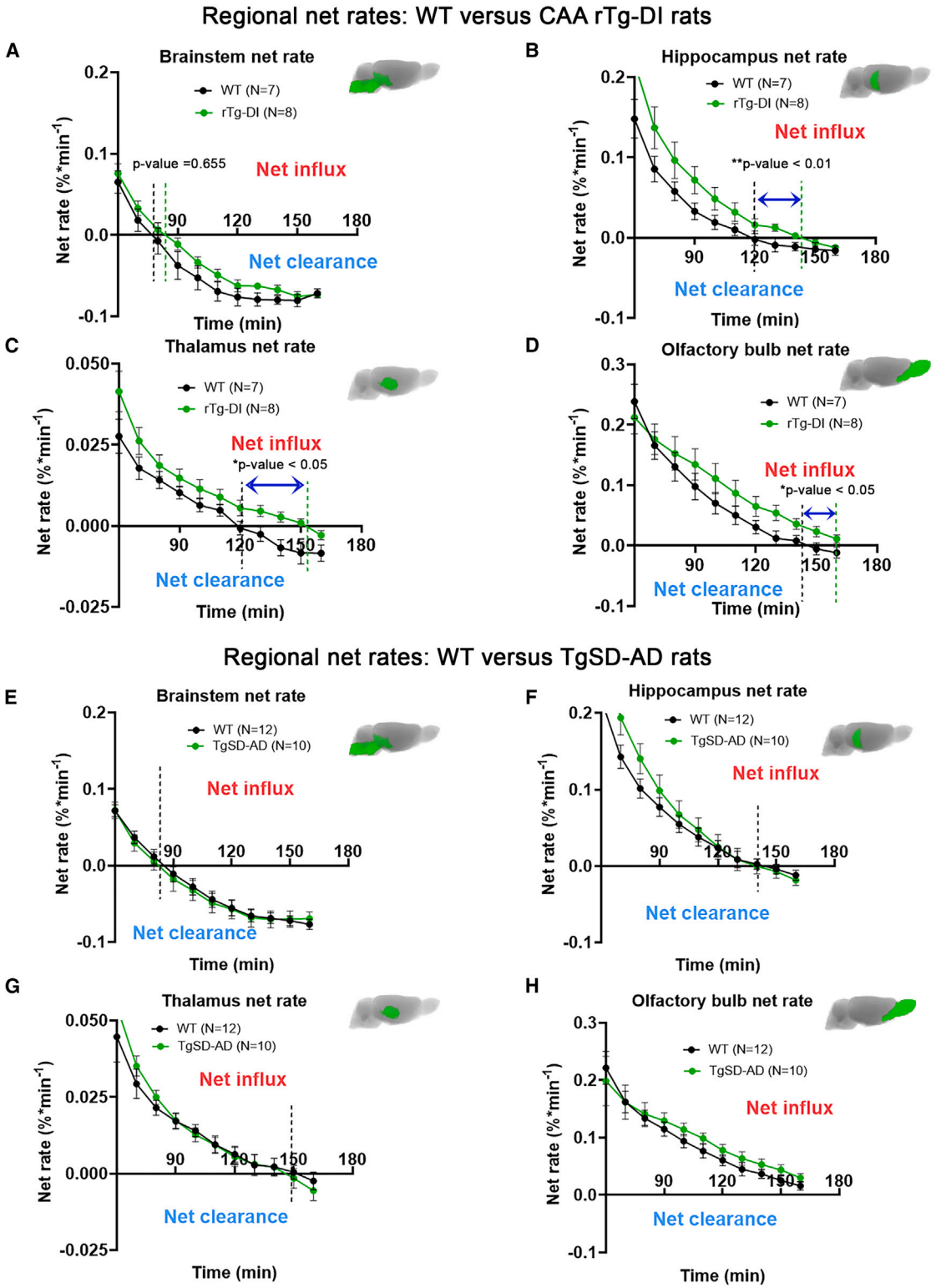

Figure 3. Divergent cerebral net rates time trajectories in CAA rTg-DI and TgSD-AD rats

(A–D) Time trajectories of the mean net rates in the brainstem, ventral hippocampus, thalamus, and olfactory bulb derived from *r-flux* brain maps from WT (black dots, $N = 7$) and rTg-DI rats (green dots, $N = 8$). The graphs depict the net rates from 60 → 160 min after CSF administration of Gd-DOTA. The dashed black and

(legend continued on next page)

rTg-DI rat CAA model maintained on a Sprague Dawley (SD) background,[30,32] we backcrossed TgF344-AD rats onto an SD background (a.k.a. "TgSD-AD" rat line) and chose to evaluate the AD rats at 12 M of age. We first validated the Aβ plaque burden in 12-month-old TgSD-AD rats using both postmortem high-resolution T2*-weighted (T2*W) MRI[41] and immunohistochemistry. Figure 4A shows a T2*W image at the level of the ventral hippocampus with multiple low-signal intensity spots scattered in the cortex and hippocampus, some of which were directly matched to fibrillar Aβ plaques on the corresponding histological section (Figure 4A, white boxes). Pixel classification was used to quantify the Aβ plaque load via calculation of the Aβ plaque area fraction, and T2*W MRI estimates correlated to that defined by immunohistochemistry via Amytracker 520 staining (R^2 = 0.443, *p*-value <0.001) (Figure 4B). Further analysis revealed that the ventral hippocampus exhibited an Aβ plaque area fractional burden of ~3% (Figure 4C) in agreement with observations of a moderate Aβ plaque burden reported in 16-month-old TgF344-AD rats.[40] To evaluate the presence of tauopathy, we performed histology using Congo red (fibrillar Aβ plaque) with CP-13 anti-p-tau antibody immunostaining and confirmed phosphorylated tau in dystrophic neurites surrounding the central Aβ core in the hippocampus as well as in the cortex of 12–14-month-old TgSD-AD rats, both of which were absent in WT rats (Figure S2). We also harvested CSF from TgSD-AD and WT rats to measure Tau-PT217 and Tau-PT181 utilizing nanoneedle technology developed by Liang and colleagues.[42] Tau-PT217 was detectable in the CSF of WT and TgSD-AD rats and revealed an increasing trend in TgSD-AD rats relative to WT control rats (Figure S2). From these data we concluded that the TgSD-AD rat line indeed exhibited AD-like pathology.

We next performed DCE-MRI with CSF Gd-DOTA administration on cohorts of 12-month-old WT (*N* = 12) and age-matched TgSD-AD rats (*N* = 10). Briefly, for these experiments the rats were anesthetized similarly to the WT/CAA cohorts, and Gd-DOTA (1:37 dilution) was administered into the CSF via the cisterna magna during DCE-MRI imaging.[11,37] The DCE-MRI data were analyzed by urOMT according to Figure 1. The binary influx/clearance maps of the whole brain showed that the WT and TgSD-AD rats exhibited similar temporal patterns of influx and clearance, implying that glymphatic transport was unchanged (representative time series examples of a WT rat and a TgSD-AD rat are shown in Figures 4D and 4E, respectively). The analysis of the regional time-varying fractional volume trends of influx and clearance focused on the brainstem, ventral hippocampus, and thalamus. In agreement with the inspection of the whole brain maps, there were no statistical differences in the regional fractional influx/clearance time trends across WT and TgSD-AD rats (Figures 4F-M). In the ventral hippocampus, time-trajectories of clearance were slowly increasing for both WT and TgSD-AD rats and the statistical LMM-RM analysis did not reveal statistically significant time*group interaction effects neither for influx nor clearance. We also compared regional net rates time-trajectories across the WT and TgSD-AD rats. The time-trends in net rates from the brainstem, ventral hippocampus, thalamus, and olfactory bulb were similar across groups implying that the transport kinetics were within normal range in the 12-month-old TgSD-AD rats (Figures 3E–3H). Finally, we assessed the regional transport in the brain tissue of the WT and TgSD-AD rats using the traditional Gd-DOTA uptake measures[8,13,19,38,39] which confirmed that there were no statistically significant differences in glymphatic transport in the preselected ROIs including in the ventral hippocampus (Figure S3). From this data, we concluded that the moderate Aβ plaque burden observed in 12-month-old TgSD-AD as such did not change glymphatic transport kinetics as defined by the urOMT analysis.

DISCUSSION

Solute clearance in the brain ISF space is technically difficult to measure *in vivo* and is an important metric to capture in studies of glymphatic system function.[13,15,16,43–48] In the current study, we implemented urOMT analysis to analyze DCE-MRI brain data to gain more information on the rates of glymphatic influx and clearance at the local tissue level. Specifically, we applied the urOMT model[27] to analyze DCE-MRI data acquired in two different rat models of neurodegenerative disease involving Aβ to characterize how parenchymal Aβ plaques in the transgenic TgSD-AD rat model and microvascular Aβ in the CAA rTg-DI rat model influence glymphatic solute influx and clearance kinetics. According to the urOMT data analysis, in normal rats, clearance emerged first in the brainstem and progressed along the base of the brain toward the olfactory bulb. Furthermore, in the normal brain, regional analysis showed that the time-trajectories of influx and clearance varied across brain regions and were most rapid in the brainstem. The urOMT analysis of the DCE-MRI data acquired from rTg-DI rats with severe CAA type 1[11,30-32] revealed impaired glymphatic influx/clearance kinetics. Specifically, in the hippocampus and thalamus where microvascular Aβ deposits are most severe in the 9-month-old rTg-DI rats[32] solute clearance was significantly time-delayed when compared to WT rats. In TgSD-AD rats glymphatic influx and clearance kinetics were within normal range including in the ventral hippocampus which exhibited a moderate burden of Aβ plaques as well as tauopathy. The urOMT results were supported by conventional measures of Gd-DOTA uptake in the preselected regions which exhibited similar trends of impaired transport in rTg-DI rats but not in TgSD-AD rats. Specifically, the TSC curves indicated a 'right-shift' in the ventral hippocampus, thalamus and olfactory bulb of CAA rTg-DI compared to WT rats interpreted as a time-delay in glymphatic transport in the CAA cohort. Similarly, the urOMT net clearance time trajectories showed a right-shift i.e., a time-delay for when net clearance exceeds net influx in the rTg-DI rats compared to WT rats. The TSC data do not by themselves contain detailed information on influx and clearance rate kinetics at the local level but support the

green lines indicate the time where the net rate = 0. The blue arrows indicate the time delay across WT and rTg-DI rats for the hippocampus, thalamus, and olfactory bulb.

(E–H) Corresponding net rates from the WT (back dots, *N* = 12) and TgSD-AD (green dots, *N* = 10) rats. The black dashed lines indicate the time when the net rate = 0. Data are mean ± SEM. **p*-value <0.05; ***p*-value <0.01.

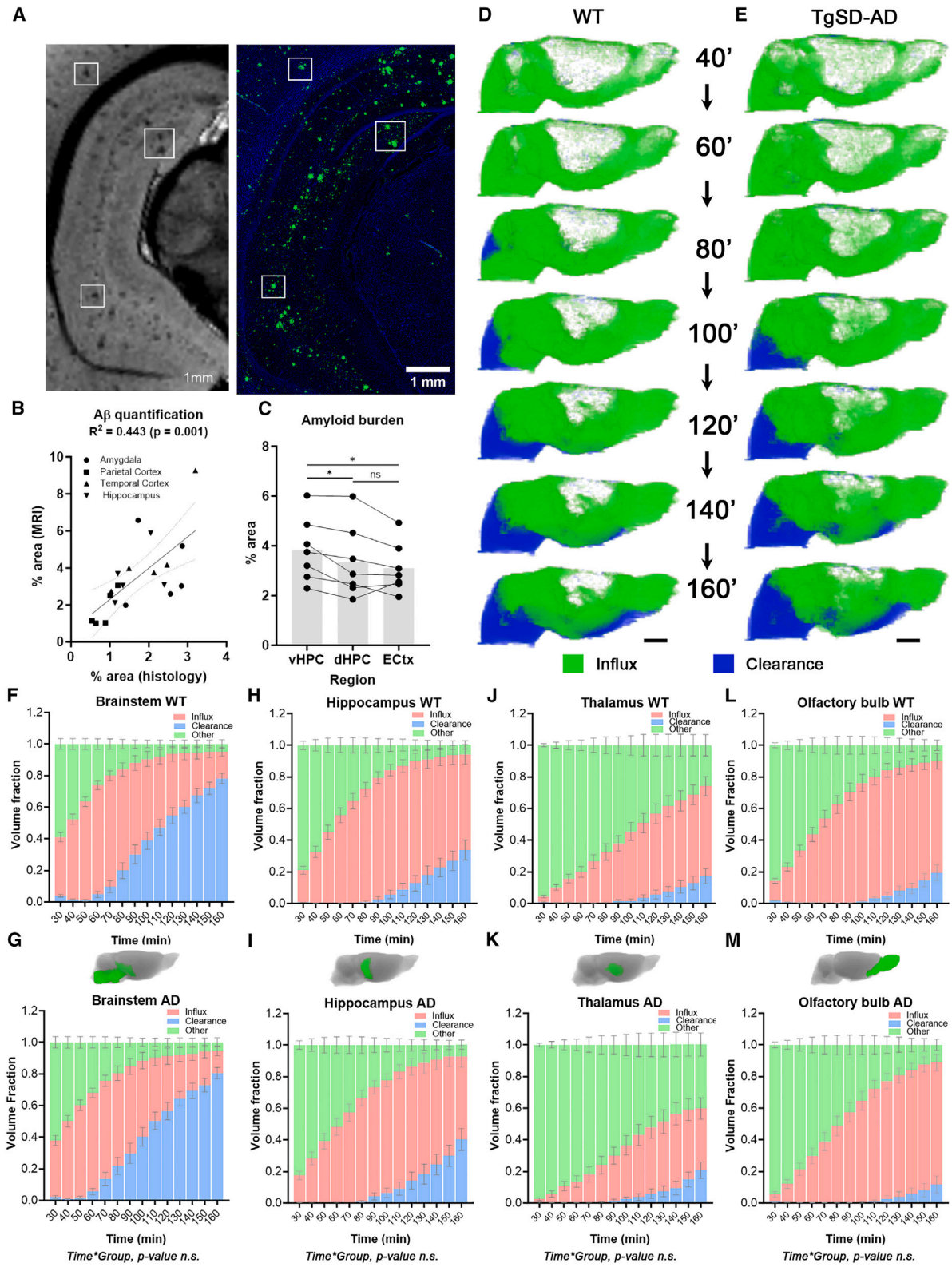

(legend on next page)

urOMT derived results that glymphatic transport kinetics are different across the two rat models. Given that this is the first time we applied the urOMT model analysis, we discuss in more detail the spatiotemporal trends of influx/clearance in normal rats. The urOMT analysis showed that influx exceeded clearance for the first ~60 min after Gd-DOTA injection. The binary maps revealed that the time-varying influx/clearance patterns varied across brain regions that might be linked to the DCE-MRI approach wherein Gd-DOTA is administered into the CSF compartment via the cisterna magna.[21] Accordingly, the Gd-DOTA tracer will follow major bulk-flow driven CSF flow streams and move from the subarachnoid space into the perivascular spaces for exchange with ISF and will therefore first encounter brain regions closer to the large subarachnoid cisterns. In support, the brainstem located in close proximity to the basal cisterns exhibited the fastest time-to-peak of influx compared to the ventral hippocampus and thalamus. Similarly, in the brainstem clearance appeared at ~60 min while at ~90 min in the hippocampus and thalamus. Faster egress of solute and fluid from tissue near the skull base could also be a result of stronger subarachnoid CSF bulk-flow near the large cistern and the aqueduct which according to the mixing hypothesis would act as a sink for diffusion driven solute clearance.[14,49–52] Although limited information is currently available, an alternative explanation of early solute clearance in the brainstem might also be related to differences in vascular factors including neurovascular coupling and spontaneous intrinsic rhythms in this region compared to other brain regions.[53] It is also noteworthy that brain regions located near the skull base may be favorably positioned for faster tissue clearance in lieu of large lymphatic networks located in near the cavernous sinus, the palate and nasopharynx.[18,54–56]

The ability to track solute clearance is of particular interest to the field of "neurofluids" and "glymphatics" in the context of the brain's ability to clear waste solutes accumulating in the ISF via this pathway.[57,58] Impairment of the glymphatic system has been linked to neurodegenerative processes including aging,[19] AD,[4] CAA[26] and normal pressure hydrocephalus.[59,60] We previously investigated age-dependent glymphatic transport function in rTg-DI rats using the DCE-MRI approach and used rOMT analysis to derive solute transport metrics including solute speed.[11] In the previous study we did not report on clearance from the brain parenchyma but instead measured drainage of GadoSpin-P from the CSF/brain to the cervical lymph nodes and observed that drainage to the deep cervical lymph nodes was time delayed in the CAA rTg-DI rats.[11] In this study, using the urOMT approach, we were able to detect glymphatic transport impairment of both influx and clearance in CAA rTg-DI rats including in brain regions in which microvascular fibrillar Aβ deposits are severe.[30,31] The decrease in glymphatic transport kinetics are likely due to the accumulating microvascular Aβ deposits as well as other pathology,[30,31] impaired vasomotion[61] and diversion of CSF away from the glymphatic system.[26] When compared to WT rats, the urOMT analysis revealed that glymphatic transport kinetics was within normal range in TgSD-AD rats even in the ventral hippocampus exhibiting a moderate Aβ plaque burden. Our results of normal influx/clearance kinetics in the transgenic AD rat model are in opposition to a previous report in APPswe/PS1dE9 (APP/PS1) mice wherein glymphatic clearance of soluble Aβ was observed to be reduced,[4] however, this apparent discrepancy is likely to be rodent model and age dependent. First, the APPswe/PS1dE9 (APP/PS1) mouse model develops Aβ plaques as early as 4 M of age and CAA pathology additionally emerges at 6 M and both lesions progresses over time.[62] The APPswe/PS1dE9 (APP/PS1) mouse model is therefore a more 'aggressive' AD (and CAA) model when compared to the TgSD-AD rat model used in our study. Second, it is possible that the DCE-MRI data and urOMT analysis approach was insensitive to track glymphatic transport changes in the setting of only moderate fibrillar Aβ pathology in the 12-month-old TgSD-AD rats. Notably, we used 12-month-old WT and TgSD-AD rats, and it is possible that abnormalities in glymphatic transport would have emerged in older TgSD-AD cohorts with more severe AD pathology. However, given that the rTg-DI and TgSD-AD rat models develop Aβ related pathologies including vascular CAA on different time scales, our current study cannot fully address the 'independent' impact of each pathology on glymphatic system function, and this will need to be further corroborated by including different time-points of the two models as well as rat models of mixed pathologies. This was beyond the scope of the current work but are planned in future study designs.

Evaluation of the urOMT model and its application to the rat brain DCE-MRI data

The motivation for developing the urOMT model and adding an additional source variable into the previous rOMT formulation

Figure 4. Hippocampal Aβ plaques in TgSD-AD rats is not linked to impaired transport

(A) T2*-weighted MRI image of ventral hippocampus from a TgSD-AD rat and corresponding histological section stained with Amytracker 520 for Aβ (slice thickness = 50μm). White boxes indicate where the location of 'spots' on MRI correspond to Aβ plaques on histology. Scale bars = 1mm.

(B) Linear regression analysis confirms that Aβ as by defined by T2*-weighted MRI correlates with histology. N = 5 animals, 4 regions per animal. Each symbol represents 1 region of interest from 1 animal. Black line represents line of best fit for all data points with 95% confidence band (R^2 = 0.443, p-value = 0.001).

(C) Amyloid beta burden across individual rats and brain regions of 12-month-old TgSD-AD rats. *Adjusted p-value <0.05. Lines connect data points from the same animal. Gray bars represent the mean value for each region. ECtx = entorhinal cortex. Amyg = amygdala. dHPC = dorsal hippocampus. PCtx = parietal cortex.

(D) Representative time series of binary maps from a 12-month-old WT showing changes in the tissue volume exhibiting influx (green) or clearance (blue).

(E) Corresponding binary influx/clearance tissue volume maps from a representative age-matched TgSD-AD rat. Scale bars = 3mm.

(F–M) Graphs showing the time-trajectories of influx and clearance as fractional volumes of the region of interest including brainstem, hippocampus, thalamus, and olfactory bulb across WT (N = 12), TgSD-AD (N = 10). The fractional volume data are group averages ±SEM. For each region, p-values for group*time interaction effects for influx and clearance were analyzed using a linear mixed model for repeated measures with independent variables including strain, time and the time × strain interaction were fit to compare the mean differences of different outcomes between strains and between time points are indicated below the graphs. ns = non-significant.

Table 1. Overview of experimental cohorts studied

Cohorts	Objective	CSF analysis	Histology
9M, female WT (*N* = 9)* and female rTg-DI (*N* = 8) rats	• Analyze new DCE-MRI data with urOMT model	No	Representative histology from a 9M rTg-DI rat was used for confirmation of microvascular Aβ
12M WT female (*N* = 11) and TgSD-AD female (*N* = 10) rats	• Analyze new DCE-MRI data with urOMT model • Postmortem MRI for assessment of Aβ plaque & corresponding histology	No	TgSD-AD (*N* = 4) WT (*N* = 3)
12-14M male WT (*N* = 4), and TgSD-AD (*N* = 4) male rats	Harvest and analyze CSF for Tau-PT217.	Yes	No

M = months, WT = Wild type rats, urOMT = unbalanced regularized optimal transport, *DCE-MRI data from two WTs rat were excluded from the analysis due to technical issues with catheter insertion and very low CSF uptake of Gd-DOTA. rTg-DI rats express human Swedish/Dutch/Iowa vasculotropic mutant amyloid-beta precursor protein (AβPP) and at 9M develop severe cerebral amyloid angiopathy represented by microvascular deposition of fibrillar amyloid beta (Aβ). The TgSD-AD rat line is a transgenic model of Alzheimer's Disease which at 12M have fibrillar Aβ plaques as well as tauopathy.

is straightforward, i.e., the DCE-MRI data are inherently unbalanced. The term "unbalanced" here refers to the non-conservation of the tracer concentration over time which is reflected by the time curve of DCE-MRI signals (Figures S1 and S3). The DCE-MRI time signal curves show that initially the Gd-DOTA uptake is rapidly rising, then reaching a plateau and slowly declining which are interpreted as the initial influx and clearance of Gd-DOTA in the tissue after being administered into the CSF. The initial rOMT model assumes that the total amount of tracer was unchanged over time and was applied to a time-window where the tracer levels were relatively stable. This limitation was remedied by the urOMT model via a source term to account for the variation of the total tracer amount within the whole brain. An advantage of the urOMT model is that it assesses the uptake (influx) and decay (clearance) of the tracer at each voxel, and also quantifies the cross-voxel exchange contributed by advection and diffusion. This is achieved by adding a source variable *r* into the advection-diffusion equation in fluid dynamics. In Vinje et al. (2023),[63] they used a similar equation to simulate the fluid transport in human brains where their source variable was also the solute clearance rate at the minute scale. The source variable can alternatively be viewed as an imaginary parallel channel where the tracer can enter and exit the system at each voxel freely. This seemingly bold assumption is motivated partly based on the current lack of knowledge pertaining to the exact anatomical routes that solutes and fluid exit the brain parenchyma and partly by the data-driven nature of the approach. The urOMT model attempts to solve an inverse problem, i.e., inferring the (apparent) local transport of a given tracer in between the DCE-MRI snapshots acquired at a temporal resolution of 5-min. The question is how to quantify continuous fluid and solute transport based on DCE-MRI images available only at discrete time points? Out of an infinite numbers of solutions, urOMT provides its own answer based on what the most likely evolving path from one image to another is by solving a predefined optimization problem.[27] Physical principles like energy minimization in the optimization problem are used to infer physically motivated flow patterns. The addition of the source term is not intended to violate the physical principle of conservation of mass. Rather, it is intended to account for (1) the known uptake of tracer during contrast injection (that cannot be precisely specified), (2) changes in signal intensity obfuscated by imaging limitations (e.g., signal strength, time resolution, etc.), (3) undiscernible movement via apparent flow, (4) efflux during contrast clearance (that cannot be precisely specified), and (5) noise control. Thus, given the inherent nature of discrete image acquisitions with DCE-MRI and the associated mathematical and technical difficulties related to modeling local influx/clearance, a most important value of the urOMT model is its applicability to analyze any given DCE-MRI dataset of individual rats for inter or cross group analyses.

Limitations of the study

The mathematical model employed in the present work, the urOMT model, is naturally defined in a fluid dynamics framework and is a data-driven model for solving the inverse problem. In other words, the transport between two images is a "black box" and urOMT model derives the most plausible evolution from one DCE-MRI image frame to another under conditions of certain assumptions: (1) the transport is governed by advection, diffusion, and influx/clearance and (2) the transport dynamics always progress in a manner that the "total transportation cost" is minimal. As is formulated in STAR Methods and Chen et al.,[27] there are two parameters in the urOMT model controlling the balance among the solute/fluid flow, influx/clearance, and the fitting of the data. For example, the extent to which cross-voxel transport is penalized relative to the instantaneous influx/clearance is controlled by the parameter α in the urOMT formulation. It is inherently challenging to determine or "tune" the optimal parameters, but understanding how the model works and utilizing well-established flow behaviors in anatomical regions (e.g., bulk flow along major arteries) informs parameter selection. In principle, alpha should be low enough to encourage mass transport (via advection/diffusion) but large enough to avoid spurious overfitting of the data and noise which would result in chaotic pathways. Thus, the α is selected to obtain the balance, yielding

strong, physically reasonable flow patterns consistent with known glymphatic transport where the source term accounts for the apparent uptake/clearance of tracer at the voxel level, as captured by the DCE-MRIs. Additionally, we have found the model to be robust with respect to α, meaning the results do not vary drastically with small changes to α.[27] Currently, we tune α based on the time-signal curves derived from the DCE-MRI data (see STAR Methods section). Another limitation of our study, as mentioned in Discussion, is that the location where the tracer enters/clears the brain is unknown. Specifying the location where influx/clearance is allowed is not straightforward given that the temporal resolution of DCE-MRI is in minutes and the anatomical exit routes of the glymphatic brain fluids are still under investigation. In additional to the limitations in temporal and spatial resolution, experimental artifacts, such as the restricted detectable ranges of signal strength, further obfuscate the true underlying physical flow, which contributes to the apparent appearance/disappearance of contrast throughout the brain region. Therefore, the source term is not spatially restricted to a particular region and is allowed to occur everywhere in the analyzed domain during the numerical simulation. In the future, a finer tuning of the model parameters (perhaps involving some machine learning techniques) is expected; a phantom experiment to test the robustness of the urOMT model applied to brain fluid kinetics is also planned. It is also important to note that we only used female rats in our study due to technical limitations (i.e., the bore size of the 9.4T MRI instrument used prohibits studies of large adult male rats with body weights greater than 500g). Thus, as such, the *in vivo* results reported in our study cannot be generalized to the male gender. Finally, we wish to highlight the limitation of the CAA rTg-DI rat model used in our study wherein cerebral Aβ deposition occurs along the capillaries (CAA type 1) and not in the wall of cortical and leptomeningeal arteries observed in the more clinically relevant sporadic CAA type 2 pathology. Specifically, autopsy studies performed in individuals with AD found mild-to-severe sporadic (non-hereditary) CAA in 79.2% and moderate-to-severe CAA in 47.5%.[64] Thus, characterizing glymphatic transport kinetics in a CAA type 2 rat model without and without co-occurring AD would have been more clinically informative. We plan to incorporate more clinically relevant CAA and mixed dementia rat models in future studies to better understand how different Aβ lesions affect glymphatic transport kinetics.

RESOURCE AVAILABILITY

Lead contact

Further information and requests for resources should be directed to and will be fulfilled by the lead contact Helene Benveniste (helene.benveniste@yale.edu).

Materials availability

The study did not generate new materials.

Data and code availability

- All data reported in this paper will be shared by the lead contact upon request.
- This paper does not report original code. The original code can be found here at https://zenodo.org/records/7839019; https://doi.org/10.5281/zenodo.7839019
- Any additional information required to reanalyze the data reported in this paper is available from the lead contact upon request.

ACKNOWLEDGMENTS

This work was supported by a grant from the Cure Alzheimer's Fund (BEE consortium), National Institutes of Health/National Institute on Aging, AG053991 (H.B., A.T., and W.E.V.N.), and NCCIH 1R01AT011419-01 (Benveniste/Tannenbaum). In addition, Z.G. was supported by grant T32GM086287 from the National Institute of General Medical Sciences.

AUTHOR CONTRIBUTIONS

Conceptualization, H.B., A.T., and R.E.; Methodology, W.E.V.N., F.L., Z.X., S.K., and H.B.; Software, X.C., R.E., K.X., and S.K.; Formal Analysis, S.K., Z. G., F.L., H.B., H.-M.L., X.C., and K.X.; Investigation, S.K., F.L., Z. G., H.L., and F.X.; Writing – Original Draft, H.B., X.C., and S.K.; Writing – review and editing, H.B., R.E., S.K., W.E.V.N., H.-M.L., X.C., and X.G.; Funding Acquisition, H.B., A.T., and W.E.V.N.; Resources, W.E.V.N., F.L., Z.X., H.B., S.K., Z. G., and H.-M.L.; Supervision, H.B., A.T., H.-M.L., and W.E.V.N.

DECLARATION OF INTERESTS

The authors declare no competing financial interests.

STAR★METHODS

Detailed methods are provided in the online version of this paper and include the following:

- KEY RESOURCES TABLE
- EXPERIMENTAL MODEL AND STUDY PARTICIPANTS DETAILS
  - Ethics and animals
- MODEL DETAILS
  - The mathematical model details
- METHOD DETAILS
  - Animal anesthesia and preparation for imaging
  - Dynamic contrast enhanced MRI (DCE-MRI) experiments
  - *In vitro* magnetic resonance imaging on postmortem brain specimens
  - Cerebrospinal fluid collection
  - Immunohistochemistry (IHC) for Aβ
  - p-Tau histology
  - Nanoneedle analysis of Tau-PT217 in cerebrospinal fluid
  - Image registration and normalization of urOMT r-flux brain maps
  - Quantification of regional Gd-uptake
  - Quantification of Aβ burden in histological and postmortem T2* MRI images
- QUANTIFICATION AND STATISTICAL ANALYSIS

SUPPLEMENTAL INFORMATION

Supplemental information can be found online at https://doi.org/10.1016/j.isci.2024.111463.

Received: April 18, 2024
Revised: July 5, 2024
Accepted: November 20, 2024
Published: November 23, 2024

REFERENCES

1. Alafuzoff, I., Arzberger, T., Al-Sarraj, S., Bodi, I., Bogdanovic, N., Braak, H., Bugiani, O., Del-Tredici, K., Ferrer, I., Gelpi, E., et al. (2008). Staging of neurofibrillary pathology in Alzheimer's disease: a study of the BrainNet Europe Consortium. Brain Pathol. *18*, 484–496. https://doi.org/10.1111/j.1750-3639.2008.00147.x.

2. Braak, H., and Braak, E. (1995). Staging of Alzheimer's disease-related neurofibrillary changes. Neurobiol. Aging *16*, 271–284. https://doi.org/10.1016/0197-4580(95)00021-6.

3. Thal, D.R., Ghebremedhin, E., Rüb, U., Yamaguchi, H., Del Tredici, K., and Braak, H. (2002). Two types of sporadic cerebral amyloid angiopathy. J. Neuropathol. Exp. Neurol. *61*, 282–293.

4. Peng, W., Achariyar, T.M., Li, B., Liao, Y., Mestre, H., Hitomi, E., Regan, S., Kasper, T., Peng, S., Ding, F., et al. (2016). Suppression of glymphatic fluid transport in a mouse model of Alzheimer's disease. Neurobiol. Dis. *93*, 215–225. https://doi.org/10.1016/j.nbd.2016.05.015.

5. Tarasoff-Conway, J.M., Carare, R.O., Osorio, R.S., Glodzik, L., Butler, T., Fieremans, E., Axel, L., Rusinek, H., Nicholson, C., Zlokovic, B.V., et al. (2015). Clearance systems in the brain-implications for Alzheimer disease. Nat. Rev. Neurol. *11*, 457–470. https://doi.org/10.1038/nrneurol.2015.119.

6. Harrison, I.F., Ismail, O., Machhada, A., Colgan, N., Ohene, Y., Nahavandi, P., Ahmed, Z., Fisher, A., Meftah, S., Murray, T.K., et al. (2020). Impaired glymphatic function and clearance of tau in an Alzheimer's disease model. Brain *143*, 2576–2593. https://doi.org/10.1093/brain/awaa179.

7. Ben-Nejma, I.R.H., Keliris, A.J., Vanreusel, V., Ponsaerts, P., Van der Linden, A., and Keliris, G.A. (2023). Altered dynamics of glymphatic flow in a mature-onset Tet-off APP mouse model of amyloidosis. Alzheimer's Res. Ther. *15*, 23. https://doi.org/10.1186/s13195-023-01175-z.

8. Da Mesquita, S., Louveau, A., Vaccari, A., Smirnov, I., Cornelison, R.C., Kingsmore, K.M., Contarino, C., Onengut-Gumuscu, S., Farber, E., Raper, D., et al. (2018). Functional aspects of meningeal lymphatics in ageing and Alzheimer's disease. Nature *560*, 185–191. https://doi.org/10.1038/s41586-018-0368-8.

9. Carare, R.O., Bernardes-Silva, M., Newman, T.A., Page, A.M., Nicoll, J.A.R., Perry, V.H., and Weller, R.O. (2008). Solutes, but not cells, drain from the brain parenchyma along basement membranes of capillaries and arteries: significance for cerebral amyloid angiopathy and neuroimmunology. Neuropathol. Appl. Neurobiol. *34*, 131–144. https://doi.org/10.1111/j.1365-2990.2007.00926.x.

10. Weller, R.O., Massey, A., Kuo, Y.M., and Roher, A.E. (2000). Cerebral amyloid angiopathy: accumulation of A beta in interstitial fluid drainage pathways in Alzheimer's disease. Ann. N. Y. Acad. Sci. *903*, 110–117. https://doi.org/10.1111/j.1749-6632.2000.tb06356.x.

11. Chen, X., Liu, X., Kounda, S., Elkin, R., Zhu, X., Monte, B., Xu, F., Pedram, M., Lee, H., Kipnis, J., et al. (2022). Cerebral amyloid angiopathy is associated with glymphatic transport reduction and time-delayed solute drainage along the neck arteries. Nature Aging *2*, 214–233. https://doi.org/10.1038/s43587-022-00181-4.

12. Bohr, T., Hjorth, P.G., Holst, S.C., Hrabětová, S., Kiviniemi, V., Lilius, T., Lundgaard, I., Mardal, K.A., Martens, E.A., Mori, Y., et al. (2022). The glymphatic system: Current understanding and modeling. iScience *25*, 104987. https://doi.org/10.1016/j.isci.2022.104987.

13. Iliff, J.J., Wang, M., Liao, Y., Plogg, B.A., Peng, W., Gundersen, G.A., Benveniste, H., Vates, G.E., Deane, R., Goldman, S.A., et al. (2012). A paravascular pathway facilitates CSF flow through the brain parenchyma and the clearance of interstitial solutes, including amyloid beta. Sci. Transl. Med. *4*, 147ra111. https://doi.org/10.1126/scitranslmed.3003748.

14. Zhao, L., Tannenbaum, A., Bakker, E.N.T.P., and Benveniste, H. (2022). Physiology of Glymphatic Solute Transport and Waste Clearance from the Brain. Physiology *37*, 349–362. https://doi.org/10.1152/physiol.00015.2022.

15. Aspelund, A., Antila, S., Proulx, S.T., Karlsen, T.V., Karaman, S., Detmar, M., Wiig, H., and Alitalo, K. (2015). A dural lymphatic vascular system that drains brain interstitial fluid and macromolecules. J. Exp. Med. *212*, 991–999. https://doi.org/10.1084/jem.20142290.

16. Louveau, A., Smirnov, I., Keyes, T.J., Eccles, J.D., Rouhani, S.J., Peske, J.D., Derecki, N.C., Castle, D., Mandell, J.W., Lee, K.S., et al. (2015). Structural and functional features of central nervous system lymphatic vessels. Nature *523*, 337–341. https://doi.org/10.1038/nature14432.

17. Thomas, J.L., and Benveniste, H. (2023). CSF-to-dura gateways. J. Exp. Med. *220*, e20221719. https://doi.org/10.1084/jem.20221719.

18. Jacob, L., de Brito Neto, J., Lenck, S., Corcy, C., Benbelkacem, F., Geraldo, L.H., Xu, Y., Thomas, J.M., El Kamouh, M.R., Spajer, M., et al. (2022). Conserved meningeal lymphatic drainage circuits in mice and humans. J. Exp. Med. *219*, e20220035. https://doi.org/10.1084/jem.20220035.

19. Kress, B.T., Iliff, J.J., Xia, M., Wang, M., Wei, H.S., Zeppenfeld, D., Xie, L., Kang, H., Xu, Q., Liew, J.A., et al. (2014). Impairment of paravascular clearance pathways in the aging brain. Ann. Neurol. *76*, 845–861. https://doi.org/10.1002/ana.24271.

20. Mestre, H., Hablitz, L.M., Xavier, A.L., Feng, W., Zou, W., Pu, T., Monai, H., Murlidharan, G., Castellanos Rivera, R.M., Simon, M.J., et al. (2018). Aquaporin-4-dependent glymphatic solute transport in the rodent brain. Elife *7*, e40070. https://doi.org/10.7554/eLife.40070.

21. Benveniste, H., Lee, H., Ozturk, B., Chen, X., Koundal, S., Vaska, P., Tannenbaum, A., and Volkow, N.D. (2021). Glymphatic Cerebrospinal Fluid and Solute Transport Quantified by MRI and PET Imaging. Neuroscience *474*, 63–79. https://doi.org/10.1016/j.neuroscience.2020.11.014.

22. Iliff, J.J., Lee, H., Yu, M., Feng, T., Logan, J., Nedergaard, M., and Benveniste, H. (2013). Brain-wide pathway for waste clearance captured by contrast-enhanced MRI. J. Clin. Invest. *123*, 1299–1309. https://doi.org/10.1172/JCI67677.

23. Ratner, V., Gao, Y., Lee, H., Elkin, R., Nedergaard, M., Benveniste, H., and Tannenbaum, A. (2017). Cerebrospinal and interstitial fluid transport via the glymphatic pathway modeled by optimal mass transport. Neuroimage *152*, 530–537. https://doi.org/10.1016/j.neuroimage.2017.03.021.

24. Elkin, R., Nadeem, S., Haber, E., Steklova, K., Lee, H., Benveniste, H., and Tannenbaum, A. (2018). GlymphVIS: Visualizing glymphatic transport pathways using regularized optimal transport. Med. Image Comput. Comput. Assist. Interv. *11070*, 844–852. https://doi.org/10.1007/978-3-030-00928-1_95.

25. Koundal, S., Elkin, R., Nadeem, S., Xue, Y., Constantinou, S., Sanggaard, S., Liu, X., Monte, B., Xu, F., Van Nostrand, W., et al. (2020). Optimal Mass Transport with Lagrangian Workflow Reveals Advective and Diffusion Driven Solute Transport in the Glymphatic System. Sci. Rep. *10*, 1990. https://doi.org/10.1038/s41598-020-59045-9.

26. Chen, X., Liu, X., Koundal, S., Elkin, R., Zhu, X., Monte, B., Xu, F., Dai, F., Pedram, M., Lee, H., et al. (2022). Cerebral amyloid angiopathy is associated with glymphatic transport reduction and time-delayed solute drainage along the neck arteries. Nat. Aging *2*, 214–223. https://doi.org/10.1038/s43587-022-00181-4.

27. Chen, X., Benveniste, H., and Tannenbaum, A.R. (2024). Unbalanced regularized optimal mass transport with applications to fluid flows in the brain. Sci. Rep. *14*, 1111. https://doi.org/10.1038/s41598-023-50874-y.

28. Eide, P.K., Vinje, V., Pripp, A.H., Mardal, K.A., and Ringstad, G. (2021). Sleep deprivation impairs molecular clearance from the human brain. Brain *144*, 863–874. https://doi.org/10.1093/brain/awaa443.

29. Ringstad, G., Valnes, L.M., Dale, A.M., Pripp, A.H., Vatnehol, S.A.S., Emblem, K.E., Mardal, K.A., and Eide, P.K. (2018). Brain-wide glymphatic enhancement and clearance in humans assessed with MRI. JCI Insight *3*, e121537. https://doi.org/10.1172/jci.insight.121537.

30. Davis, J., Xu, F., Hatfield, J., Lee, H., Hoos, M.D., Popescu, D., Crooks, E., Kim, R., Smith, S.O., Robinson, J.K., et al. (2018). A Novel Transgenic Rat Model of Robust Cerebral Microvascular Amyloid with Prominent Vasculopathy. Am. J. Pathol. *188*, 2877–2889. https://doi.org/10.1016/j.ajpath.2018.07.030.

31. Zhu, X., Hatfield, J., Sullivan, J.K., Xu, F., and Van Nostrand, W.E. (2020). Robust neuroinflammation and perivascular pathology in rTg-DI rats, a novel model of microvascular cerebral amyloid angiopathy. J. Neuroinflammation *17*, 78. https://doi.org/10.1186/s12974-020-01755-y.

32. Lee, H., Xu, F., Liu, X., Koundal, S., Zhu, X., Davis, J., Yanez, D., Schrader, J., Stanisavljevic, A., Rothman, D.L., et al. (2021). Diffuse white matter loss in a

transgenic rat model of cerebral amyloid angiopathy. J. Cerebr. Blood Flow Metabol. *41*, 1103–1118. https://doi.org/10.1177/0271678X20944226.

33. Schrader, J.M., Stanisavljevic, A., Xu, F., and Van Nostrand, W.E. (2022). Distinct Brain Proteomic Signatures in Cerebral Small Vessel Disease Rat Models of Hypertension and Cerebral Amyloid Angiopathy. J. Neuropathol. Exp. Neurol. *81*, 731–745. https://doi.org/10.1093/jnen/nlac057.

34. Schrader, J.M., Xu, F., Lee, H., Barlock, B., Benveniste, H., and Van Nostrand, W.E. (2022). Emergent White Matter Degeneration in the rTg-DI Rat Model of Cerebral Amyloid Angiopathy Exhibits Unique Proteomic Changes. Am. J. Pathol. *192*, 426–440. https://doi.org/10.1016/j.ajpath.2021.11.010.

35. Popescu, D.L., Van Nostrand, W.E., and Robinson, J.K. (2020). Longitudinal Cognitive Decline in a Novel Rodent Model of Cerebral Amyloid Angiopathy Type-1. Int. J. Mol. Sci. *21*, 2348. https://doi.org/10.3390/ijms21072348.

36. Schrader, J.M., Xu, F., Agostinucci, K.J., DaSilva, N.A., and Van Nostrand, W.E. (2024). Longitudinal markers of cerebral amyloid angiopathy and related inflammation in rTg-DI rats. Sci. Rep. *14*, 8441. https://doi.org/10.1038/s41598-024-59013-7.

37. Ozturk, B., Koundal, S., Al Bizri, E., Chen, X., Gursky, Z., Dai, F., Lim, A., Heerdt, P., Kipnis, J., Tannenbaum, A., et al. (2023). Continuous positive airway pressure increases CSF flow and glymphatic transport. JCI Insight *8*, e170270. https://doi.org/10.1172/jci.insight.170270.

38. Hablitz, L.M., Plá, V., Giannetto, M., Vinitsky, H.S., Stæger, F.F., Metcalfe, T., Nguyen, R., Benrais, A., and Nedergaard, M. (2020). Circadian control of brain glymphatic and lymphatic fluid flow. Nat. Commun. *11*, 4411. https://doi.org/10.1038/s41467-020-18115-2.

39. Eide, P.K., and Ringstad, G. (2015). MRI with intrathecal MRI gadolinium contrast medium administration: a possible method to assess glymphatic function in human brain. Acta Radiol. Open *4*, 2058460115609635. https://doi.org/10.1177/2058460115609635.

40. Cohen, R.M., Rezai-Zadeh, K., Weitz, T.M., Rentsendorj, A., Gate, D., Spivak, I., Bholat, Y., Vasilevko, V., Glabe, C.G., Breunig, J.J., et al. (2013). A transgenic Alzheimer rat with plaques, tau pathology, behavioral impairment, oligomeric abeta, and frank neuronal loss. J. Neurosci. *33*, 6245–6256. https://doi.org/10.1523/JNEUROSCI.3672-12.2013.

41. Benveniste, H., Einstein, G., Kim, K.R., Hulette, C., and Johnson, G.A. (1999). Detection of neuritic plaques in Alzheimer's disease by magnetic resonance microscopy. Proc. Natl. Acad. Sci. USA *96*, 14079–14084. https://doi.org/10.1073/pnas.96.24.14079.

42. Liang, F., Baldyga, K., Quan, Q., Khatri, A., Choi, S., Wiener-Kronish, J., Akeju, O., Westover, M.B., Cody, K., Shen, Y., et al. (2023). Preoperative Plasma Tau-PT217 and Tau-PT181 Are Associated With Postoperative Delirium. Ann. Surg. *277*, e1232–e1238. https://doi.org/10.1097/SLA.0000000000005487.

43. Cserr, H.F., Cooper, D.N., Suri, P.K., and Patlak, C.S. (1981). Efflux of radiolabeled polyethylene glycols and albumin from rat brain. Am. J. Physiol. *240*, F319–F328. https://doi.org/10.1152/ajprenal.1981.240.4.F319.

44. Szentistvanyi, I., Patlak, C.S., Ellis, R.A., and Cserr, H.F. (1984). Drainage of interstitial fluid from different regions of rat brain. Am. J. Physiol. *246*, F835–F844. https://doi.org/10.1152/ajprenal.1984.246.6.F835.

45. Lee, H., Xie, L., Yu, M., Kang, H., Feng, T., Deane, R., Logan, J., Nedergaard, M., and Benveniste, H. (2015). The Effect of Body Posture on Brain Glymphatic Transport. J. Neurosci. *35*, 11034–11044. https://doi.org/10.1523/JNEUROSCI.1625-15.2015.

46. Benveniste, H., Lee, H., Ding, F., Sun, Q., Al-Bizri, E., Makaryus, R., Probst, S., Nedergaard, M., Stein, E.A., and Lu, H. (2017). Anesthesia with Dexmedetomidine and Low-dose Isoflurane Increases Solute Transport via the Glymphatic Pathway in Rat Brain When Compared with High-dose Isoflurane. Anesthesiology *127*, 976–988. https://doi.org/10.1097/Aln.0000000000001888.

47. Pla, V., Bork, P., Harnpramukkul, A., Olveda, G., Ladron-de-Guevara, A., Giannetto, M.J., Hussain, R., Wang, W., Kelley, D.H., Hablitz, L.M., and Nedergaard, M. (2022). A real-time in vivo clearance assay for quantification of glymphatic efflux. Cell Rep. *40*, 111320. https://doi.org/10.1016/j.celrep.2022.111320.

48. Ray, L., Iliff, J.J., and Heys, J.J. (2019). Analysis of convective and diffusive transport in the brain interstitium. Fluids Barriers CNS *16*, 6. https://doi.org/10.1186/s12987-019-0126-9.

49. Bakker, E.N.T.P., Naessens, D.M.P., and VanBavel, E. (2019). Paravascular spaces: entry to or exit from the brain? Exp. Physiol. *104*, 1013–1017. https://doi.org/10.1113/EP087424.

50. Davson, H. (1976). Review lecture. The blood-brain barrier. J. Physiol. *255*, 1–28. https://doi.org/10.1113/jphysiol.1976.sp011267.

51. Aktas, G., Kollmeier, J.M., Joseph, A.A., Merboldt, K.D., Ludwig, H.C., Gärtner, J., Frahm, J., and Dreha-Kulaczewski, S. (2019). Spinal CSF flow in response to forced thoracic and abdominal respiration. Fluids Barriers CNS *16*, 10. https://doi.org/10.1186/s12987-019-0130-0.

52. Dreha-Kulaczewski, S., Joseph, A.A., Merboldt, K.D., Ludwig, H.C., Gärtner, J., and Frahm, J. (2015). Inspiration is the major regulator of human CSF flow. J. Neurosci. *35*, 2485–2491. https://doi.org/10.1523/JNEUROSCI.3246-14.2015.

53. Chan, S.T., Evans, K.C., Song, T.Y., Selb, J., van der Kouwe, A., Rosen, B.R., Zheng, Y.P., Ahn, A.C., and Kwong, K.K. (2020). Dynamic brain-body coupling of breath-by-breath O2-CO2 exchange ratio with resting state cerebral hemodynamic fluctuations. PLoS One *15*, e0238946. https://doi.org/10.1371/journal.pone.0238946.

54. Ma, Q., Ineichen, B.V., Detmar, M., and Proulx, S.T. (2017). Outflow of cerebrospinal fluid is predominantly through lymphatic vessels and is reduced in aged mice. Nat. Commun. *8*, 1434. https://doi.org/10.1038/s41467-017-01484-6.

55. Ahn, J.H., Cho, H., Kim, J.H., Kim, S.H., Ham, J.S., Park, I., Suh, S.H., Hong, S.P., Song, J.H., Hong, Y.K., et al. (2019). Meningeal lymphatic vessels at the skull base drain cerebrospinal fluid. Nature *572*, 62–66. https://doi.org/10.1038/s41586-019-1419-5.

56. Yoon, J.H., Jin, H., Kim, H.J., Hong, S.P., Yang, M.J., Ahn, J.H., Kim, Y.C., Seo, J., Lee, Y., McDonald, D.M., et al. (2024). Nasopharyngeal lymphatic plexus is a hub for cerebrospinal fluid drainage. Nature *625*, 768–777. https://doi.org/10.1038/s41586-023-06899-4.

57. Nedergaard, M. (2013). Neuroscience. Garbage truck of the brain. Science *340*, 1529–1530. https://doi.org/10.1126/science.1240514.

58. Nedergaard, M., and Goldman, S.A. (2016). Brain Drain. Sci. Am. *314*, 44–49. https://doi.org/10.1038/scientificamerican0316-44.

59. Ringstad, G., Vatnehol, S.A.S., and Eide, P.K. (2017). Glymphatic MRI in idiopathic normal pressure hydrocephalus. Brain *140*, 2691–2705. https://doi.org/10.1093/brain/awx191.

60. Eide, P.K., Valnes, L.M., Pripp, A.H., Mardal, K.A., and Ringstad, G. (2020). Delayed clearance of cerebrospinal fluid tracer from choroid plexus in idiopathic normal pressure hydrocephalus. J. Cerebr. Blood Flow Metabol. *40*, 1849–1858. https://doi.org/10.1177/0271678X19874790.

61. van Veluw, S.J., Hou, S.S., Calvo-Rodriguez, M., Arbel-Ornath, M., Snyder, A.C., Frosch, M.P., Greenberg, S.M., and Bacskai, B.J. (2020). Vasomotion as a Driving Force for Paravascular Clearance in the Awake Mouse Brain. Neuron *105*, 549–561.e5. https://doi.org/10.1016/j.neuron.2019.10.033.

62. Garcia-Alloza, M., Robbins, E.M., Zhang-Nunes, S.X., Purcell, S.M., Betensky, R.A., Raju, S., Prada, C., Greenberg, S.M., Bacskai, B.J., and Frosch, M.P. (2006). Characterization of amyloid deposition in the APPswe/PS1dE9 mouse model of Alzheimer disease. Neurobiol. Dis. *24*, 516–524. https://doi.org/10.1016/j.nbd.2006.08.017.

63. Vinje, V., Zapf, B., Ringstad, G., Eide, P.K., Rognes, M.E., and Mardal, K.A. (2023). Human brain solute transport quantified by glymphatic MRI-informed biophysics during sleep and sleep deprivation. Fluids Barriers CNS *20*, 62. https://doi.org/10.1186/s12987-023-00459-8.

64. Jakel, L., De Kort, A.M., Klijn, C.J.M., Schreuder, F., and Verbeek, M.M. (2022). Prevalence of cerebral amyloid angiopathy: A systematic review and meta-analysis. Alzheimers Dement *18*, 10–28. https://doi.org/10.1002/alz.12366.

65. Tustison, N.J., Avants, B.B., Cook, P.A., Zheng, Y., Egan, A., Yushkevich, P.A., and Gee, J.C. (2010). N4ITK: improved N3 bias correction. IEEE Trans. Med. Imag. *29*, 1310–1320. https://doi.org/10.1109/TMI.2010.2046908.

66. Percie du Sert, N., Hurst, V., Ahluwalia, A., Alam, S., Avey, M.T., Baker, M., Browne, W.J., Clark, A., Cuthill, I.C., Dirnagl, U., et al. (2020). The ARRIVE guidelines 2.0: Updated guidelines for reporting animal research. BMC Vet. Res. *16*, 242. https://doi.org/10.1186/s12917-020-02451-y.

67. Rathi, Y., Olver, P., Sapiro, G., and Tannenbaum, A. (2006). Affine invariant surface evolutions for 3D image segmentation. Proc. SPIE *6064*, 606401. https://doi.org/10.1117/12.640282.

68. Johnson, G.A., Calabrese, E., Badea, A., Paxinos, G., and Watson, C. (2012). A multidimensional magnetic resonance histology atlas of the Wistar rat brain. Neuroimage *62*, 1848–1856. https://doi.org/10.1016/j.neuroimage.2012.05.041.

69. Johnson, G.A., Cofer, G.P., Gewalt, S.L., and Hedlund, L.W. (2002). Morphologic phenotyping with MR microscopy: the visible mouse. Radiology *222*, 789–793. https://doi.org/10.1148/radiol.2223010531.

70. Davis, J., Xu, F., Miao, J., Previti, M.L., Romanov, G., Ziegler, K., and Van Nostrand, W.E. (2006). Deficient cerebral clearance of vasculotropic mutant Dutch/Iowa Double A beta in human A betaPP transgenic mice. Neurobiol. Aging *27*, 946–954. https://doi.org/10.1016/j.neurobiolaging.2005.05.031.

71. Xu, F., Grande, A.M., Robinson, J.K., Previti, M.L., Vasek, M., Davis, J., and Van Nostrand, W.E. (2007). Early-onset subicular microvascular amyloid and neuroinflammation correlate with behavioral deficits in vasculotropic mutant amyloid beta-protein precursor transgenic mice. Neuroscience *146*, 98–107. https://doi.org/10.1016/j.neuroscience.2007.01.043.

72. Jung, S.S., and Van Nostrand, W.E. (2002). Abeta does not induce oxidative stress in human cerebrovascular smooth muscle cells. Neuroreport *13*, 1309–1312.

73. McKay, T.B., Qu, J., Liang, F., Mueller, A., Wiener-Kronish, J., Xie, Z., and Akeju, O. (2022). Tau as a serum biomarker of delirium after major cardiac surgery: a single centre case-control study. Br. J. Anaesth. *129*, e13–e16. https://doi.org/10.1016/j.bja.2022.04.002.

74. Barriere, D.A., Magalhaes, R., Novais, A., Marques, P., Selingue, E., Geffroy, F., Marques, F., Cerqueira, J., Sousa, J.C., Boumezbeur, F., et al. (2019). The SIGMA rat brain templates and atlases for multimodal MRI data analysis and visualization. Nat. Commun. *10*, 5699. https://doi.org/10.1038/s41467-019-13575-7.

75. Bankhead, P., Loughrey, M.B., Fernández, J.A., Dombrowski, Y., McArt, D.G., Dunne, P.D., McQuaid, S., Gray, R.T., Murray, L.J., Coleman, H.G., et al. (2017). QuPath: Open source software for digital pathology image analysis. Sci. Rep. *7*, 16878. https://doi.org/10.1038/s41598-017-17204-5.

76. Paxinos, G., and Watson, C. (1997). The Rat Brain in Stereotaxic Coordinates, 3rd Edition (Academic Press).

STAR★METHODS

KEY RESOURCES TABLE

REAGENT or RESOURCE	SOURCE	IDENTIFIER
Antibodies		
Goat polyclonal Collagen IV	Novus Biologicals, LLC	NBP1-26549; RRID: AB_1853202
Amytracker 520	Ebba Biotech AB	RRID: AB_3665890
Hoechst33342	Abcam	ab228551; RRID: AB_3665889
Mouse mAb CP-13	gift from Dr. Peter Davies*	N/A
Biotinylated secondary antibody	Vectastain Elite ABC-HRP kit, Vector Laboratories	RRID: AB_3665891
Thioflavin S	Sigma-Aldrich	T1892; RRID: AB_3665892
Chemicals, peptides, and recombinant proteins		
Formalin solution, neutral buffered, 10%	Sigma-Aldrich	HT501128-4L
Heparin sodium	Sagent Pharmaceuticals	NDC 25021-400-30
Diaminobenzidine solution	Sigma-Aldrich	D5905
Congo Red	Sigma-Aldrich	HT60
Tris-based antigen unmasking solution	Vector Laboratories	H-3301-250
3% hydrogen peroxidase		
Super blocker buffer	Invitrogen	
Ketamine (KETASET)	Zoetis Inc.	NDC 54771-2013-1
Xylazine	Akorn Inc.	NDC 59399-111-50
Dexmedetomidine (Dexdomotor)	Zoetis Inc.	NDC 54771-2805-1
Isoflurane, USP	Covetrus	NDC 11695-6777-2
Cyanoacrylate glue (Loctite)	Henkel Co.	LOC-230992
Susceptibility-matched fluid (Galden)	TMC industries	HT230
Gadoteric acid (DOTAREM)	Guerbet LLC	NDC 67684-2000-3
Experimental models: Organisms/strains		
rTg-DI rats	Dr. Van Nostrand, URI	Davis et al.[30]
TgF344-AD rats		Cohen et al.[40]
Sprague Dawley (SD)	Dr. Van Nostrand, URI	
Software and algorithms		
Unbalanced regularized optimal mass transport	Xinan Chen	https://zenodo.org/records/7839019
IBM SPSS Statistics, Version 26		
MATLAB	MathWorks, Natick, MA, USA	R2017a
SPM 12	The Wellcome Trust Center for Neuroimaging at University College London (UCL)	http://www.fil.ion.ucl.ac.uk/spm
N4 bias field correction algorithm		Tustison et al.[65]
PMOD	PMOD Technologies LLC, Zürich, Switzerland	PMOD, version 3.908
Paravision 6.1 software	Bruker BioSpin, Billerica, MA, USA	
Qupath v0.3.2	Qupath	https://qupath.github.io/

EXPERIMENTAL MODEL AND STUDY PARTICIPANTS DETAILS

Ethics and animals

All experiments involving the use of animals for the research were approved by the by the local institutional animal care and use committees at URI, Rhode Island, USA (study approval number: AN-1718-008) and Yale University, New Haven, USA (study approval number: 2022–20132). Female hemizygous rTg-DI CAA type 1 rat line (Sprague Dawley (SD) background), which expresses human

Swedish/Dutch/Iowa vasculotropic mutant amyloid-beta precursor protein (AβPP) under control of the neuronal Thy1.2 promoter and produces chimeric Dutch/Iowa CAA mutant Aβ peptides in brain were bred and maintained at the University of Rhode Island (URI).[30,31,35] Separate cohorts of the in-house bred rTg-DI female rats and non-transgenic female littermates (serving as WT controls) were used at 9-month (M) of age. For AD, we used a transgenic rat model of AD which develops both Aβ plaques and tauopathy. Specifically, we imported TgF344-AD rats[40] from the Rat Resource and Research Center (Strain: F344-Tg(Prp-APP,Prp-PS1)19/Rrrc, Columbia, MO, USA). The Tg344-AD rat line expresses mutant human amyloid precursor protein (APPsw) and presenilin 1 (PS1ΔE9) genes, both under transcriptional control of a mouse prion promoter.[40] The imported TgF344-AD rats, on Fisher 344 background, were subsequently bred onto a Sprague Dawley (SD) background for >8 generations (hereby designated "TgSD-AD") at the University of Rhode Island (URI). This was performed to better relate the AD data to those obtained in CAA which was based on the hemizygous rTg-DI CAA type 1 rat line created on an SD background.[11] Separate cohorts of the in-house bred TgSD-AD female and male rats and normal SD wild-type (WT) non-transgenic littermates were used for the experiments at 11-14 months-of-age. The rats were transported from URI to Yale University at least 4–6 weeks prior to scheduled DCE-MRI imaging or other experimentation. Details of the species/strain, genotype, age and gender for each cohort is reported in Table 1. At Yale, the rats were housed in an environment with controlled temperature, individually ventilated cages, and humidity, 12/12 h light cycle from 7:00 a.m. to 7:00 p.m. and fed standard chow and water *ad libitum*. We adhered to the essential ARRIVE guidelines[66] for reporting the animal research presented.

MODEL DETAILS

The mathematical model details

Previously in the rOMT model, only advection and diffusion were included in the formulation and a constraint of total mass conservation was assumed.[11,37] Consequently, rOMT was only suitable for analysis of a time window of DCE-MRI data during which the total tracer level was relatively stable (e.g., ∼60 min after Gd-DOTA infusion) so that the total mass conservation constraint was approximately satisfied. The urOMT model employed in this work allows solute exchange between the brain and the outside region by adding a source variable into its mathematical formulation as an imaginary "channel" of tracer entering and exiting. As a result, the urOMT model can be applied during a broader DCE-MRI experimental time window where the total concentration of the tracer may fluctuate over time, or in other words, is unbalanced.[27] Due to the data-driven nature of the urOMT model, which infers apparent flow behavior from apparent changes in signal between images, the source term accounts for apparent uptake/clearance of tracer as detected at the voxel-level.

The urOMT model used in the present work is formulated as follows. Given initial and final density functions $\rho_0(x) \geq 0$ and $\rho_1(x) \geq 0$ defined on a bounded set $\Omega \subseteq \mathbb{R}^3$, one solves the problem:

$$\min_{\rho,v,r} \int_0^T \int_\Omega \left(\rho(t,x) \| v(t,x) \|^2 + \alpha \rho(t,x) r(t,x)^2 \right) dxdt$$

subject to

$$\begin{cases} \frac{\partial \rho}{\partial t} + \nabla \bullet (\rho v) = \sigma \Delta \rho + \rho r, (1) \\ \rho(0,x) = \rho_0(x), \rho(T,x) = \rho_1(x). \end{cases} \quad \text{(Equation 1)}$$

Here $\rho(t,x) : [0,T] \times \Omega \to \mathbb{R}^+$, $v(t,x) : [0,T] \times \Omega \to \mathbb{R}^3$ and $r(t,x) : [0,T] \times \Omega \to \mathbb{R}$ are spatiotemporal density function, velocity field and relative source variable, respectively; $\sigma > 0$ is the constant diffusion coefficient; $\alpha > 0$ is the weighting parameter of the source term in the cost function. This model takes inputs $\rho_0(x)$ and $\rho_1(x)$, and solves for the optimal $\rho(t,x), v(t,x)$ and $r(t,x)$ transporting $\rho_0(x)$ into $\rho_1(x)$. The partial differential Equation 1 is called the unbalanced advection-diffusion equation in fluid dynamics and incorporates transport motions of advection (bulk flow), diffusion and source of quantities. A positive r gives the rate of influx of per unit mass per unit of time into the system and a negative r for that of clearance. The boundary condition for solving the partial differential Equation 1 is the Neumann boundary condition which means the normal derivative of the variables at the spatial boundary is 0. To apply urOMT to the acquired DCE-MRI data, we assume that the % signal change from baseline of DCE-MRI is proportional to the concentration of the tracer, which thus can be represented by the density function in the urOMT formulation. Further, when considering the urOMT formulation as described above, the choice of the weighting parameter α is crucial since it controls how "unbalanced" the system is. We note that the smaller the weighting parameter α is, the less the source term is penalized, and the easier it is for the relative source to gain or lose mass.[27] In the present study, in order to account for the rapid increase in solute concentration based on the time signal curves of the DCE-MRI images, we initially implement a small α value to allow the relative source to play a more dominant role in the system. Then, after reaching an approximate steady state, we transition to a larger value of α (Figure S4). For continuity, we smoothed the resulting piecewise constant function with a Gaussian filter to create a slowly increasing α sequence.

In context of glymphatic solute transport, Equation 1 expresses that the total transport process is governed by three types of transport motions of the Gd-tagged tracer: advection, diffusion, and influx/clearance. These three motions independently contribute to the

total transport as manifested by the image data and in the domain of 3D DCE-MRI image data, the three motions individually happen at the same time within each voxel. Specifically, advection and diffusion together account for cross-voxel transport. In contrast, the source-term accounts for influx/clearance of tracer where local movement cannot be inferred and is thus quantified at each local voxel level with r representing the rate of influx per unit mass per unit time and ρr representing the rate per unit time. The positive or negative sign of ρr (or equivalently of r) indicates whether it is influx or clearance *dominated*, respectively, for each voxel. The absolute value of ρr indicates the "strength" or intensity of influx or clearance of the tracer locally.

In the following, we detail on the computational pipeline of the entire urOMT analysis of the DCE-MRI data. First, a 3D affine denoising filter[67] was applied to the parametric % signal change from baseline DCE-MRI images to smooth the image noise but preserve the edges. For each rat, the time series of 3D DCE-MRI images were fed into the urOMT model by running the algorithm between each pair of adjacent images, which returned 14 dynamic 10-min time averaged *r-flux* (ρr) maps. The *r-flux* maps provide spatial and temporal quantification of the *net* amount of influx (if positive) and clearance (if negative) per unit time. For simplicity of visualizing the spatial changes in influx/clearance, binary influx/clearance maps were derived by setting voxels with $\rho r > 0.0001$ as influx voxels and those with $\rho r < -0.0001$ as clearance voxel. Several scalar metrics can be further derived from each of the above maps to characterize the regional influx and clearance properties in a given region of the brain. From the binary influx/clearance maps, the influx volume fraction (the influx volume in mm^3 divided by total volume of the region in mm^3), clearance volume fraction (the clearance volume in mm^3 divided by total volume of the region in mm^3) and 'other' volume fraction (the volume where $-0.0001 \leq \rho r \leq -0.0001$ in mm^3 divided by total volume of the region in mm^3) can be calculated. From the r-flux maps, the net rate can also be calculated defined as the spatial average of all ρr values within a region. A zero net rate is considered as influx rates and clearance rates being evenly matched. To connect in the time dimension, we derived the time-trajectories of these metrics by calculating them at all time points for analysis across groups.

METHOD DETAILS

Animal anesthesia and preparation for imaging

All rats underwent anesthesia and surgery during their light cycle in a counter-balanced manner across strains and CSF administration of Gd-DOTA and DCE-MRI imaging was performed similar to previously reported experiments.[11,46] Briefly, anesthesia included induction with 3% isoflurane, followed by a bolus of dexmedetomidine (0.01 mg/kg i.p.) mixed with glycopyrrolate (0.02 mg/kg i.p.). Surgical plane anesthesia was established and maintained with 2–3% isoflurane delivered via a nose cone in a 1:1 Air:O_2 mixture. For surgery, the rats were position in a stereotaxic frame, and a small copper tube (0.32 mm o.d., Nippon Tockushukan, MFG. CO., LTD, Tokyo, Japan) connected to a PE 10 catheter was positioned into the CSF compartment via the cisterna magna (CM) and secured in place using cyanoacrylate glue. After surgery, the anesthetized rat was transferred to the 9.4T MRI instrument. During imaging, anesthesia was maintained by a subcutaneous continuous infusion of dexmedetomidine at a rate of 0.009 mg/kg/h supplemented with 1–1.2% isoflurane delivered at an FiO2 of 50%. Throughout the experiments, vital signs including pulse oximetry, heart rate, respiratory rate and body temperature were monitored using non-invasive MRI compatible monitors (SA Instruments, Stony Brook, NY, USA).

Dynamic contrast enhanced MRI (DCE-MRI) experiments

For imaging on the 9.4T MRI instrument we used a custom-made transmit RF coil (50-mm i.d.) for signal excitation and a 3-cm surface radiofrequency (RF) loop coil (Bruker), positioned under the head of the rat was used as a receiver. First, we acquired anatomical proton-density weighted (PDW) images at the level of the head using a 3D Fast low angle shot (FLASH) sequence with the following parameters: TR/TE/FA/number of averages = 15 m/4 m/7°/2, scanning time = 13.5 min, resolution = 0.23 × 0.23 × 0.23 mm^3. Following this, serial T1-weighted images were acquired using a 3D FLASH sequence with the following parameters: TR/TE/FA/number of averages = 15 m/4 m/15°/2, scan time = 5 min, resolution = 0.3 × 0.3 × 0.3 mm^3). Specifically, three baseline 3D FLASH images were acquired prior to contrast infusion followed by post-contrast 3D FLASH T1-weighted scans acquired continuously for 160 min. For all whole-brain glymphatic DCE-MRI experiments, 30μL of 1:37 gadoteric acid (Gd-DOTA, DOTAREM, Guerbert LLC, Carol Stream IL) diluted in sterile water was infused at a rate of 1.5μL/min into the CSF using a syringe pump (Legato 130 Nanoliter, kd Scientific).

In vitro magnetic resonance imaging on postmortem brain specimens

To characterize the burden of Aβ plaque deposition in TgSD-AD rats, we acquired 3D multiple gradient echo (MGE) *ex vivo* high spatial resolution T2*-weighted MRI imaging techniques on a subset of the brains from the 12M old WT (N = 3) and TgSD-AD (N = 4) rats (Table 1). For these experiments, the rats underwent the active gadolinium staining technique to improve the signal-to-noise ratio.[68,69] Specifically, for the staining technique procedure, the rats received an i.p., overdose of ketamine (~200 mg/kg) with xylazine (~10 mg/kg) where after they underwent transcardial perfusion fixation with a mixture of phosphate buffer 4% paraformaldehyde solution (SF-100 Fischer Scientific) containing 5% (50 mM) Gd-DOTA (Guerbet LLC, Princeton, NJ, USA) delivered by a servo-controlled peristaltic pump (Masterflex Peristaltic Tubing Pumps, Cole-Parmer, Vernon Hills, IL, USA). Following perfusion-fixation the rat's head was then decapitated, excess muscles around of skull removed, and the skull intact specimen was stored in the PBS+-Gd-DOTA mixture at 4°C for at least 7 days. Prior to imaging, the specimens were allowed to reach room temperature (19°C–21°C) before being placed in a custom-made specimen holder containing proton signal-free susceptibility-matched fluid (Galden

Heat Transfer Fluids, HT230. Kurt J. Lesker, Company, USA). MRI acquisitions were performed on a Bruker 9.4 T/16 cm bore MRI instrument with a BGA-9S-HP imaging gradient interfaced to a Bruker Avance III console and controlled by Paravision 6.1 software (Bruker BioSpin, Billerica, MA, USA). A volume RF transmit and receive coil with an inner diameter of 4.0 cm was utilized and a 3D MGE imaging protocol was implemented using the following parameters: TR = 60 m; TE = 5, 12, 19, 26 ms; number of averages = 7; FOV = 32 × 20 × 20; acquisition matrix 462 × 308 × 308; isotropic voxel resolution of 65 μm × 65 μm × 65 μm, requiring a total acquisition time of 11 h 5 min per specimen. All the individual echo images were summed together for the analysis of Aβ plaques burden (see below for more details of quantification of Aβ plaque burden). The summed T2* MRI brain images were imported into PMOD (PMOD, version 3.908, PMOD Technologies LLC, Zürich, Switzerland) to screen for the presence and distribution pattern of spot-like signal hypo-intensities in the hippocampus.

Cerebrospinal fluid collection

As shown in Table 1, CSF from a separate series of anesthetized 12-14 month-old male TgSD-AD (N = 4) and WT (N = 4) rats was collected via a catheter positioned in the cisterna magna.[11] The anesthesia regimen was the same as used for the DCE-MRI studies. Approximately 150μL of CSF was collected per animal, which was utilized for both quantification of phosphorylated Tau at threonine 217 (Tau-PT217) using the newly-established nanoneedle technology.[42]

Immunohistochemistry (IHC) for Aβ

Following MRI imaging experiments, the rats were injected with an i.p. overdose of ketamine/xylazine (∼200 mg/kg and∼10 mg/kg) and subsequently underwent intracardially perfusion fixation with heparinized 0.01M phosphate buffered saline (PBS; heparinized to 1 unit per mL) followed by 10% neutral buffered formalin (NBF). Brains were post-fixed for 48–72 h in 10% NBF, followed by cryoprotection via three equilibrations in a solution of 30% sucrose in PBS. Brains were then frozen in Tissue-Plus O.C.T. Compound (Fisher Scientific, 23-730-571) and sectioned on a CM1950 cryostat (Leica Biosystems). Serial 50μm coronal sections through the entire extent of forebrain (i.e., frontal pole to temporal pole) were collected and stored in a lab-made cryoprotectant solution consisting of 30% sucrose (Research Products International, Product #S24065–3000.0) and 50% ethylene glycol (J.T. Baker, Product # 9300-01) in 0.01M PBS. IHC processing was performed at room temperature (approximately 20°C) with light agitation except where explicitly noted otherwise. To identify Aβ free-floating coronal sections at approximately 3.6mm caudal to bregma were washed in 0.01M PBS, incubated in Amytracker 520 for 30 min (1:1000, Ebba Biotech AB), counterstained with Hoechst33342 for 5 min (5μM, Abcam, ab228551), and finally washed in 0.01M PBS. Tissue sections were slide mounted and cover slipped with VECTASHIELD Vibrance Antifade Mounting Medium (Vector Laboratories, H-1700-10), which was allowed to set for at least 12 h before imaging. No amyloid was detected in wild-type brains following Amytracker 520 labeling. The immunohistochemistry of microvascular Aβ from 9M old rTg-DI rats shown in Figure 2 were performed as previously described.[30,70–72] Specifically, fibrillar amyloid was visualized by thioflavin-S staining and cerebral blood vessels by collagen IV.

p-Tau histology

Fifty-μm-thick TgSD-AD and WT brain sections were mounted on Colorfrost Plus slides (Fisher Scientific) and rehydrated in PBS. Heat induced antigen retrieval was performed in Tris-based antigen unmasking solution (Vector Laboratories, H-3301). Endogenous peroxidase activity was blocked with 3% hydrogen peroxidase in PBS for 30 min. Non-specific binding was reduced using Super Blocker Reagent (Invitrogen) for 30 min at room temperature. Slides were incubated with mouse mAb CP-13 (1:200; a gift from Dr. Peter Davies, Litwin-Zucker Center for Research on Alzheimer's disease at the Feinstein Institute) at 4°C overnight. Slides were then washed in PBS and incubated with biotinylated anti-mouse IgG (Vector Laboratories) for 2 h at room temperature. The biotinylated secondary antibody was labeled using Vectastain Elite ABC-HRP kit (1:1000; Vector Laboratories) and visualized with stable diaminobenzidine solution (Invitrogen). After washing with PBS, slides were incubated in Alkaline Sodium Chloride solution (Sigma, HT60) for 20 min and then stained with Alkaline Congo Red solution (Sigma, HT60) for 20 min followed by rinsing in absolute ethanol, cleared in xylene and cover slipped.

Nanoneedle analysis of Tau-PT217 in cerebrospinal fluid

The collected CSF samples were centrifuged at 12000 g for 10 min to eliminate the cluster, and CSF supernatant was collected into a sample tube. Subsequently the protein concentration in the CSF sample was measured by a Nanodrop machine (Thermo Fisher Scientific, Waltham, MA). Tau-PT217 was measured by the nanoneedle platform (NanoMosaic, Waltham, MA) as described in our previous studies.[42,73] Specifically, blank nanoneedle chips supplied by NanoMosaic. 5 μg/mL capture antibody were incubated with the nanoneedle chip overnight. It was then washed in PBS and incubated in the blocking solution for 1 h. Five μL of purified CSF samples were diluted 2 X into the dilution buffer provided by NanoMosaic. The diluted sample was incubated on the chip for 2 h. After washing, 0.5 μg/mL detection antibody was incubated on the chip. We used phospho-specific antibody to Tau-PT217 (Cat#44–744, ThermoFisher) as the detection antibody. We used TessieTM instrument (NanoMosaic) to image the chip and the software provided by NanoMosaic to analyze the colors of all nanoneedles and reported the percentage of the color-shifted number of nanoneedles. The protein concentrations were reported in relative units specific to the nanoneedle technology (i.e., relative concentration (a.u.)).

DCE-MRI data were corrected for head motion, and underwent intensity normalization and smoothing with the full-width, half-maximum Gaussian smoothing kernel of 0.1 mm. The smoothened data was used to calculate the voxel-wise percent signal change from baseline as described previously.[22,45,46]

Image registration and normalization of urOMT r-flux brain maps

The registration and analysis of the processed DCE-MRI data were performed employing MATLAB based SPM12 software packages. (http://www.fil.ion.ucl.ac.uk/spm). The 3D-PDW images were co-registered and resliced to the DCE-MRI data. The co-registered/resliced PDW images were corrected for signal intensity inhomogeneity with the N4 bias field correction algorithm.[65] Each bias-field corrected PDW image was then segmented into gray matter, white matter, and CSF tissue probability maps to generate deformation fields using our custom-made tissue probability brain atlas map. The deformation fields were subsequently applied to spatially normalize individual urOMT derived 3D *r-flux* maps. The publicly available Sigma rat brain atlas[74] was normalized to our template space and edited to use preselected regions of interest including brainstem, ventral hippocampus, and the thalamus. The preselected customized atlas regions of interest (ROIs) were subsequently transformed into each rat brain's original space using the obtained normalization parameters. All spatial normalization procedures were performed using the SPM12 software package (http://www.fil.ion.ucl.ac.uk/spm). The spatially normalized regions of interest (ROIs) specific to each rat brain were subsequently utilized to analyze the corresponding urOMT dataset, enabling the calculation of influx/clearance parameters, using the publicly available FSL software packages (Jenkinson et al., 2012).

Quantification of regional Gd-uptake

From each of the parametric dynamic MRI images 'Time-Signal-Curves' (TSCs) of Gd-DOTA induced signal changes were extracted using PMOD software (PMOD Technologies Ltd, Zürich, Switzerland, version 4.2) from the regions of interest using preselected regions of interest including brainstem, ventral hippocampus, and the thalamus spatially normalized to the individual anatomical templates for each rat. Volumetric rendering of Gd-DOTA distribution at various times after CSF administration were enabled using Amira software (FEI, Thermo Fisher Scientific, OR, USA, Version 6.2).

Quantification of Aβ burden in histological and postmortem T2* MRI images

Immunofluorescent whole-section tile scans were acquired using a Zeiss Axio Imager.Z2 microscope with digital CMOS Camera (Hamamatsu Photonics, C14440-20UP), LED light source (Excelitas Technologies Corp., XT720×S), 20× Plan-Apochromat air objective (0.8 numerical aperture), and Apotome.2. Uniformity of illumination within each tile image was corrected using the "shading correction" function of Zeiss Zen software (version 3.1 Zen pro). For the proof-of-concept demonstration that MR microscopy is a suitable method for Aβ burden quantification, multiple brain regions in a single histological section per animal were analyzed and compared to corresponding section in the postmortem MRI. We analyzed variability in amyloid area fraction (AAF) between brain regions for correlation of MR microscopy with a validated marker for amyloid plaques in the brain (Amytracker 520). We examined four regions of interest (ROIs) due to their previously characterized progression of amyloid accumulation[40]: entorhinal/perirhinal cortex, amygdala, hippocampus, and parietal cortex. We differentiated between parietal cortex and entorhinal/perirhinal cortex due to apparent differences in amyloid deposition between these two subsets of cortex in all animals. Whole-section fluorescence microscopy images were analyzed in QuPath version 0.3.2.,[75] and regions of interest were manually contoured using Paxinos and Watson[76] as reference. Within QuPath, a pixel classifier was trained by an experienced experimenter to automatically identify amyloid-positive tissue versus amyloid-negative tissue throughout each ROI. Due to high signal-to-noise ratio present from Amytracker 520, classifiers applied to histological data did not appear to misclassify any tissue when examined thoroughly by experimenters and was considered ground truth for evaluation of amyloid burden though MR microscopy.

QUANTIFICATION AND STATISTICAL ANALYSIS

Sample sizes were chosen on the basis of similar experiments.[11] Data are presented as mean ± SEM unless otherwise stated. For urOMT analysis the experimenters were blinded to the identity of experimental groups until the end of data collection and analysis for all the independent experiments. For each of the preselected brain regions the urOMT time trajectories of influx/clearance volume or influx/clearance rates, as well as the TSC derived from the DCE-MRI images a linear mixed model with a heterogeneous variance covariance matrix for repeated measures with independent variables including strain (TgSD-AD vs. WT or rTg-DI vs. WT), time and the time × strain interaction were fit to compare the mean differences of different outcomes between strains and between time points after Gd-DOTA administration within each strain of rats. Group differences were calculated using a post-hoc pairwise Fisher's least significant difference (LSD) with adjustments for multiple comparisons using Bonferroni correction. Two-group comparisons were made using a two-tailed unpaired independent t-test assuming unequal variances. Details of number of animals in each cohort are listed in Table 1. All statistical analyses were performed using IBM SPSS Statistics, Version 26. A p-value of less than 0.05 was chosen to indicate statistical significance. All statistics are reported in the figure legends.